

# CMS Physics Analysis Summary

---

Contact: cms-pag-conveners-top@cern.ch

2020/05/08

## Measurement of differential $t\bar{t}$ production cross sections for high- $p_T$ top quarks in proton-proton collisions at $\sqrt{s} = 13$ TeV

The CMS Collaboration

### Abstract

A measurement of the production cross section for high transverse momentum ( $p_T$ ) top quark pairs is reported. The data set was collected during 2016 with the CMS detector at the CERN LHC from proton-proton collisions at a center-of-mass energy of 13 TeV, and corresponds to an integrated luminosity of  $35.9 \text{ fb}^{-1}$ . The measurement uses events where either both top quark candidates decay hadronically and are reconstructed as large-radius jets with  $p_T > 400 \text{ GeV}$ , or where one top quark decays hadronically and is identified as a single large-radius jet with  $p_T > 400 \text{ GeV}$  and the other top quark decays leptonically to a b jet, an electron or a muon, and a neutrino. The cross section is extracted differentially as a function of kinematic variables of the top quark or the top quark pair system. The results are presented at the particle level, within a region of phase space close to that of the experimental acceptance, and at the parton level, and are compared to various theoretical models. The measured differential cross sections are significantly lower in both decay channels in the phase space of interest, compared to the theory predictions, while the normalized differential cross sections are consistent between data and theory.



## 1 Introduction

The top quark completes the third generation of quarks in the standard model (SM), and a precise knowledge of its properties is critical for the overall understanding of the theory. Measurements of the top quark-antiquark pair ( $t\bar{t}$ ) production cross section confront the predictions from quantum chromodynamics (QCD), while being sensitive to effects of physics beyond the SM. The  $t\bar{t}$  production process is also a dominant SM background to many direct searches for new physics phenomena and therefore its detailed characterization is essential for new discoveries.

The large  $t\bar{t}$  yield expected in proton-proton (pp) collisions at the CERN LHC enables measurements of the  $t\bar{t}$  production rate in a large phase space, and more importantly, differentially, as a function of the kinematic properties of the top quark and  $t\bar{t}$  system. Such measurements have been performed by the ATLAS [1–6] and CMS [7–16] Collaborations at 7, 8, and 13 TeV center-of-mass energies, assuming a resolved final state where the decay products of the  $t\bar{t}$  pair can be reconstructed individually. This approach is possible for top quark transverse momenta  $p_T$  up to approximately 500 GeV. At higher  $p_T$ , the top quark decay products are highly collimated ("boosted") and they can no longer be reconstructed separately. In order to explore the highly boosted phase space, hadronic top quark decays are reconstructed as large-radius ( $R$ ) jets. Previous efforts in this domain by the ATLAS [17, 18] and CMS [19] Collaborations confirm that it is feasible to perform precise differential measurements of high- $p_T$   $t\bar{t}$  production and have also shown interesting deviations from the theory predictions.

In this note, a measurement of the differential boosted  $t\bar{t}$  production cross section in the hadronic and lepton+jets final states is presented, using pp collisions at  $\sqrt{s} = 13$  TeV recorded with the CMS detector during the 2016 LHC run and amounting to a total integrated luminosity of  $35.9 \text{ fb}^{-1}$ . In the hadronic decay channel, each W boson arising from the top quark decays into a pair of light quarks. As a result, the final state consists of at least six partons (more are possible due to initial- and final-state radiation), two of which are b quarks. Due to the high boost considered in this measurement ( $p_T > 400$  GeV), the top quarks are reconstructed unambiguously as large- $R$  jets and the final state consists of at least two such jets. In the lepton+jets channel, one top quark decays to a hadronically-decaying W boson and a b quark ( $t \rightarrow Wb \rightarrow q\bar{q}'b$ ) and is reconstructed as a single large- $R$  jet, while the second top quark decays to a W boson, which in turn decays to a charged lepton ( $\ell$ ), either an electron or a muon ( $e/\mu$ ), and a neutrino, together with a b quark ( $t \rightarrow Wb \rightarrow \ell v b$ ). The presented measurements are performed using a significantly larger data set compared to the previous CMS results and utilize improved reconstruction techniques, leading to reduced uncertainties, which permit a confrontation of the theoretical predictions in a wider phase space.

The note is organized as follows: Section 2 gives the details of the Monte Carlo (MC) simulations. The object reconstruction and the event selection are outlined in Sections 3 and 4, respectively. In Section 5, the estimation of the background contributions is explained, followed by a discussion of the signal extraction in Section 6. The systematic uncertainties are discussed in Section 7. The unfolding procedure used to obtain the particle- and parton-level cross sections and the resulting measurements are presented in Section 8. Finally, Section 9 provides the summary of the note.

## 2 Simulated events

MC simulation is used to generate samples for the  $t\bar{t}$  signal and to model the kinematic distributions of some of the background processes. Samples of simulated  $t\bar{t}$  events have been generated

at next-to-leading order (NLO) in QCD using POWHEG (v2) [20–24], assuming a top quark mass of  $m_t = 172.5 \text{ GeV}$ . Single top quark production in the  $t$  channel or in association with a W boson are simulated at NLO with POWHEG [25]. The production of W or Z bosons in association with jets (V+jets), as well as QCD multijet events, are simulated with MG5\_AMC@NLO [26] at leading order (LO), with the MLM matching algorithm [27]. Samples of diboson (WW, WZ, ZZ) events are simulated using PYTHIA (v8.212) [28, 29].

All simulated events are processed with PYTHIA for modeling of the parton showering, hadronization, and underlying event (UE). The NNPDF 3.0 [30] parton distribution functions (PDFs) are used throughout, and the CUETP8M1 UE tune [31] is used for all processes except for the tt and single top quark processes, for which the tune CUETP8M2T4 [32] is used. The simulation of the CMS detector response is based on GEANT4 [33]. Additional pp interactions in the same or neighboring bunch crossings (pileup) are simulated with PYTHIA and overlaid with generated events according to the pileup distribution measured in data.

The various simulated processes are normalized to the best known theoretical cross sections, namely the tt, V+jets, and single top quark samples are normalized to NNLO precision in QCD [34–36].

The measured cross sections for the tt process are compared to theoretical predictions provided by the following MC models: POWHEG combined with PYTHIA for the parton showering as described above, or combined with HERWIG++ [37] and the corresponding EE5C UE tune [38]. In addition, a comparison is performed with MC@NLO [26] using PYTHIA for the parton showering. The measured differential cross sections are additionally compared to state-of-the-art theory calculations at NNLO precision.

### 3 Object reconstruction

The global event reconstruction (also called particle-flow event reconstruction [39]) aims to reconstruct and identify each individual particle in an event, with an optimized combination of all subdetector information. In this process, the identification of the particle type (photon, electron, muon, charged hadron, neutral hadron) plays an important role in the determination of the particle direction and energy. Photons (e.g. coming from  $\pi^0$  decays or from electron bremsstrahlung) are identified as ECAL energy clusters not linked to the extrapolation of any charged particle trajectory to the ECAL. Electrons (e.g. coming from photon conversions in the tracker material, B hadron semileptonic decays, or from the decay of a vector boson) are identified as primary charged tracks linked potentially to many ECAL energy clusters, corresponding to the tracks' extrapolation to the ECAL, and to possible bremsstrahlung photons emitted along the way through the tracker material. Muons (e.g. from vector bosons or B hadron semileptonic decays) are identified as tracks in the central tracker consistent with either a track or several hits in the muon system, and associated with calorimeter deposits compatible with the muon hypothesis. Charged hadrons are identified as charged particle tracks neither identified as electrons, nor as muons. Finally, neutral hadrons are identified as HCAL energy clusters not linked to any charged hadron trajectory, or as a combined ECAL and HCAL energy excess with respect to the expected charged hadron energy deposit.

The energy of photons is obtained from the ECAL measurement. The energy of electrons is determined from a combination of the track momentum at the main interaction vertex, the corresponding ECAL cluster energy, and the energy sum of all bremsstrahlung photons attached to the track. The energy of muons is obtained from the corresponding track momentum. The energy of charged hadrons is determined from a combination of the track momentum and the

corresponding ECAL and HCAL energies, corrected for zero-suppression effects and for the response function of the calorimeters to hadronic showers. Finally, the energy of neutral hadrons is obtained from the corresponding corrected ECAL and HCAL energies.

Leptons and charged hadrons are required to be compatible with originating from the primary interaction vertex. The reconstructed vertex with the largest value of summed physics object  $p_T^2$  is taken to be the primary pp interaction vertex. The physics objects are the jets, clustered using the jet finding algorithm described below, with the tracks assigned to the vertex as inputs, and the associated missing transverse momentum, taken as the negative vector sum of the  $p_T$  of those jets. Charged hadrons that are associated with a pileup vertex are classified as pileup candidates and are ignored in the subsequent object reconstruction. Electron and muon objects are first identified from corresponding electron or muon particle-flow candidates. Next, jet clustering is performed on all particle-flow candidates that are not classified as pileup candidates. The jet clustering does not exclude the electron and muon particle-flow candidates, even if these have already been assigned to electron/muon objects. A dedicated overlap removal is therefore applied at the analysis level to avoid double counting.

Electrons and muons must have  $p_T > 50$  (20) GeV and  $|\eta| < 2.1$  for the  $\ell$ +jets channel (for vetoing leptons in the hadronic channel). Leptons are also required to be isolated according to the "mini isolation" ( $I_{\text{mini}}$ ) algorithm, which requires the  $p_T$  sum of tracks in a cone around the electron or muon to be less than a given fraction of the lepton  $p_T$  ( $p_T^\ell$ ). The cone width varies with the lepton  $p_T$  as  $\Delta R = 10/p_T^\ell$  for  $p_T^\ell < 200$  GeV and  $\Delta R = 0.05$  for  $p_T^\ell > 200$  GeV. A cut value of  $I_{\text{mini}} < 0.1$  is used. The usage of the mini-isolation algorithm retains high isolation efficiency also for leptons from boosted top quark decays. A looser lepton selection is used to define additional veto leptons in the  $\ell$ +jets channel, requiring  $p_T > 50$  GeV and  $|\eta| < 2.1$  but no isolation requirement. Correction factors are applied to account for differences between data and the simulation in the modeling of the lepton identification, isolation, and trigger efficiencies, determined as a function of the electron/muon  $|\eta|$  and  $p_T$ .

For each event, hadronic jets are clustered from the particles reconstructed by the particle-flow algorithm using the infrared and collinear safe anti- $k_T$  algorithm [40, 41]. Two different jet collections are considered for the analysis to identify b and t jet candidates, respectively. Small- $R$  jets are clustered using a distance parameter of 0.4 (used in the  $\ell$ +jets channel) and large- $R$  jets using a distance parameter of 0.8 (used in the  $\ell$ +jets and hadronic channels). The jet momentum is determined as the vectorial sum of all particle momenta in the jet, and is found from simulation to be on average within 5–10% of the true momentum over the whole  $p_T$  spectrum and detector acceptance. Additional pp pileup interactions can contribute additional tracks and calorimetric energy depositions to the jet momentum. To mitigate this effect, charged particles identified to be originating from pileup vertices are discarded and an offset correction is applied to correct for remaining contributions.

Jet energy corrections are derived from simulation studies to bring the average measured response of jets to that of particle-level jets. In situ measurements of the momentum balance in dijet, photon+jet, Z+jet, and QCD multijet events are used to account for any residual differences in the jet energy scale between data and simulation [42]. The jet energy resolution amounts typically to 15% at 10 GeV, 8% at 100 GeV, and 4% at 1 TeV. Additional selection criteria are applied to each jet to remove jets potentially dominated by anomalous contributions from various subdetector components or reconstruction failures.

In order to identify jets originating from hadronic decays of top quarks (t tagging), we use the  $N$ -subjettiness variables [43]  $\tau_3$ ,  $\tau_2$ , and  $\tau_1$  computed using the jet constituents according to

$$\tau_N = \frac{1}{\sum_k p_{T,k} R} \sum_k p_{T,k} \min\{\Delta R_{1,k}, \Delta R_{2,k}, \dots, \Delta R_{N,k}\}, \quad (1)$$

where  $N$  denotes the number of reconstructed candidate subjets and  $k$  runs over the constituent particles in the jet. The variable  $\Delta R_{i,k} = \sqrt{(\Delta y_{i,k})^2 + (\Delta \phi_{i,k})^2}$  is the angular distance between the candidate subjet  $i$  and the particle  $k$ . The variable  $R$  is the characteristic jet radius ( $R = 0.8$  in our case). The centers of hard radiation are found by performing the exclusive  $k_T$  algorithm [44, 45] on the jet constituents before the application of any grooming techniques.

In addition, a grooming technique is applied to remove soft, wide-angle radiation from the jet and to improve the mass resolution. The algorithm employed is the “modified mass drop tagger” [46, 47], also known as the *soft-drop* (SD) algorithm [48], with angular exponent  $\beta = 0$ , soft cutoff threshold  $z_{\text{cut}} < 0.1$ , and characteristic radius  $R_0 = 0.8$  [48]. The subjets within the large- $R$  jets are identified by a reclustering of their constituents with the Cambridge–Aachen algorithm [49, 50] and by reversing the last step of the clustering history.

Small- $R$  jets and subjets of the large- $R$  jets are identified as b quark candidates (b tagged) using the combined secondary vertex (CSV) algorithm [51]. Data-to-simulation correction factors are used to match the b tagging efficiency observed in simulation to that measured in data. The typical efficiency of the b tagging algorithm for small- $R$  jets (large- $R$  subjets) is 63% (58%) for true b jets, while the misidentification probability for non-b jets is 1%. For the large- $R$  subjets, the efficiency for tagging true b jets drops from 65% to 40% as the  $p_T$  increases from 20 GeV to 1 TeV.

The missing transverse momentum vector  $\vec{p}_T^{\text{miss}}$  is defined as the projection on the plane perpendicular to the beams of the negative vector sum of the momenta of all the particle-flow candidates in an event. Its magnitude is referred to as  $p_T^{\text{miss}}$ .

## 4 Event selection

### 4.1 Trigger

Different triggers were employed for the collection of signal events in the hadronic and  $\ell$ +jets channels according to each event topology. The trigger used in the hadronic channel required the presence of a jet with  $p_T > 180$  GeV at L1. At the HLT, large- $R$  jets were reconstructed from particle-flow candidates using the anti- $k_T$  algorithm with a distance parameter of 0.8. The mass of the jets at the HLT, after removal of soft particles, was required to be greater than 30 GeV. Selected events were required to contain at least two such jets with  $p_T > 280$  (200) GeV for the leading (trailing) jet. Finally, at least one of these jets was required to be b tagged, using the CSV algorithm suitably adjusted for the HLT, with an average identification efficiency of 90% for b jets. The aforementioned trigger ran for the entire 2016 run, collecting an integrated luminosity of  $35.9 \text{ fb}^{-1}$ . A second trigger with identical kinematic requirements but without any b tagging requirement was employed and ran on average every 21 bunch crossings, collecting an integrated luminosity of  $1.67 \text{ fb}^{-1}$ . The events collected with the latter trigger are used for the selection of a control data sample for estimating the QCD multijet background in the hadronic channel, as described later. For the  $\ell$ +jets channel, the data were selected using triggers requiring a single lepton, either an electron with  $p_T > 45$  GeV or a muon with  $p_T > 40$  GeV and  $|\eta| < 2.1$ , with no isolation criteria applied, as well as two small- $R$  jets with  $p_T > 200$  and 50 GeV, respectively.

## 4.2 Hadronic channel

All events considered in the hadronic channel are required to fulfill a common baseline selection. This requires the presence of at least two large- $R$  jets in the event with  $p_T > 400 \text{ GeV}$  and soft-drop masses in the range  $50\text{--}300 \text{ GeV}$ . In addition, events with at least one lepton are vetoed in order to suppress leptonic top quark decays.

In order to discriminate between events that originate from  $t\bar{t}$  decays and QCD multijet production, jet substructure variables are utilized. These variables are sensitive to the type of the jet, and in particular to whether it comes from a single-prong decay, like ordinary quark or gluon jets, or from a three-prong decay, such as the  $t \rightarrow W b \rightarrow \bar{q} q' b$  decay that is of interest here. The  $\tau_{1,2,3}$  variables of the two leading- $p_T$  large- $R$  jets are combined with a neural network (NN) to form a multivariate event discriminant that characterizes each event, with values close to zero indicating QCD dijet production and values close to one suggesting  $t\bar{t}$  production. The variables have been chosen such that the correlation with the number of b-tagged subjets, which is used to define control regions for the QCD multijet background, is minimal. The NN consists of two hidden layers with 16 and 4 nodes, respectively, and is implemented using the TMVA toolkit [?]. More complex architectures have not improved the discriminating capabilities of the NN. The training of the NN was performed with simulated QCD multijet (background) and  $t\bar{t}$  (signal) events that satisfy the baseline selection, using the back-propagation method and a sigmoid activation function for the nodes. Excellent agreement between data and simulation has been observed for the input variables in the phase space of the training.

On top of the baseline selection, sub-selection regions that serve different analysis purposes are defined based on the NN output, the soft-drop mass of the jets, and the number of b-tagged subjets in each large- $R$  jet. The signal region (SR), used to perform the differential measurements, contains events collected with the signal trigger where both large- $R$  jets have a b-tagged subjet and their masses lie in the range  $120\text{--}220 \text{ GeV}$ , while the NN output value is greater than 0.8. This value has been chosen such that the  $t\bar{t}$  signal over background ratio is large, while keeping enough signal events with top quark  $p_T$  above 1 TeV. In this region, more than 95% of the selected  $t\bar{t}$  events originate from hadronic top quark decays. The QCD multijet control region (CR) contains events collected with the control trigger that satisfy the same requirements as the SR but with the b tagging requirement inverted (the large- $R$  jets should not contain a b-tagged subjet). Additionally, expanded regions that include SR and CR are defined for estimates of the background distributions. The signal region A ( $SR_A$ ) is the same as SR with an extended requirement on the mass of the large- $R$  jets ( $50\text{--}300 \text{ GeV}$ ), while the corresponding control region ( $CR_A$ ) has the b tagging condition reverted. It should be noted that the events selected in  $SR_A$  and  $CR_A$  were collected with the signal and control triggers, respectively. Finally, the signal region B ( $SR_B$ ) is used to constrain some of the signal modeling uncertainties and has the same selection criteria as the SR but without any NN requirement.

## 4.3 Lepton+jets channel

The  $\ell + \text{jets}$  final state is identified through the presence of an electron or a muon, a small- $R$  jet assumed to be produced by the decay of the b quark from the leptonic top quark decay, and a large- $R$  jet corresponding to the hadronically decaying top quark. Small- $R$  jets are required to have  $p_T > 50 \text{ GeV}$  and  $|\eta| < 2.4$ , while large- $R$  jets must fulfill  $p_T > 400 \text{ GeV}$  and  $|\eta| < 2.4$ .

All events are required to fulfill a set of preselection criteria, defined as follows:

- Exactly one signal electron or signal muon
- Zero additional veto leptons

- At least one leptonic-side jet (small- $R$  jet in the same hemisphere as the signal lepton,  $0.3 < \Delta R(\ell, \text{jet}) < \pi/2$ )
- At least one hadronic-side jet (large- $R$  jet in the opposite hemisphere to the signal lepton,  $\Delta R(\ell, \text{jet}) > \pi/2$ )
- $p_T^{\text{miss}} > 50$  (35) GeV for the electron (muon) channel
- For events in the electron channel, a ‘triangular’ cut is required to ensure that the missing transverse momentum vector does not point along the transverse direction of the electron or the leading jet:  $|\Delta\phi(X, p_T^{\text{miss}})| < 1.5 \cdot \frac{p_T^{\text{miss}}}{7 \text{ GeV}}$ , where  $X$  stands for electron or leading small- $R$  jet

The more stringent  $p_T^{\text{miss}}$  and triangular criteria used in the electron channel are applied to further reduce background from QCD multijet production.

Events that fulfill the preselection criteria are categorized according to whether the  $b$  ( $t$ ) jet candidate passes or fails the  $b$  ( $t$ ) tagging criteria. The  $b(t)$  jet candidate is the highest- $p_T$  leptonic-side (hadronic-side) jet in the event. The  $N$ -subjettiness ratio  $\tau_3/\tau_2$  (abbreviated as  $\tau_{32}$ ) is used as the sensitive variable to distinguish a three-prong hadronic top quark decay from background processes, requiring  $\tau_{32} < 0.81$ . A data-to-simulation efficiency correction factor is extracted simultaneously with the integrated signal yield, as described in Section 6, to correct the  $t$  tagging efficiency in simulation to match that in data. Events are divided into the following categories:

- 0  $t$  tag (0t): the  $t$  jet candidate fails the  $t$  tagging requirement
- 1  $t$  tag, 0  $b$  tag (1t0b): the  $t$  jet candidate passes the  $t$  tagging requirement, but the  $b$  jet candidate fails the  $b$  tagging requirement
- 1  $t$  tag, 1  $b$  tag (1t1b): both the  $t$  jet candidate and the  $b$  jet candidate pass their respective tagging requirement

These event categories are designed to have different admixtures of signal and background, with the 0t region being the most background dominated and the 1t1b region the most signal dominated.

## 5 Background estimation

The dominant background in the hadronic channel is QCD multijet production, while in the  $\ell + \text{jets}$  channel, the dominant sources of background events include non-signal  $t\bar{t}$ , single top quark,  $W + \text{jets}$ , and QCD multijet production. Non-signal  $t\bar{t}$  production comprises dileptonic and hadronic final states, in addition to  $\tau + \text{jets}$  events where the tau lepton does not decay to an electron or a muon.

In the hadronic channel, the background due to QCD multijet production is significantly suppressed through a combination of subjet  $b$  tagging requirements and the event NN output. The remaining contribution is estimated from a control data sample. The two elements that are determined from data are the distribution  $Q(x)$  of the QCD multijet background as a function of an observable of interest  $x$ , and the absolute normalization  $N_{\text{QCD}}$ . The QCD template  $Q(x)$  is taken from the data control region  $\text{CR}_A$ . The  $t\bar{t}$  signal contamination of this control sample, based on the simulation, is of the order of 1%. The normalization of the QCD multijet background ( $N_{\text{QCD}}$ ) is determined from a maximum likelihood fit to the data in  $\text{SR}_A$  of the soft-drop mass of the  $t$  jet candidate,  $m_t^*$ , where the  $t$  jet candidate is taken as the leading- $p_T$  large- $R$  jet. The fit is described by the equation

$$D(m^t) = N_{\text{tt}} T(m^t; k_{\text{scale}}, k_{\text{res}}) + N_{\text{QCD}}(1 + k_{\text{slope}} m^t) Q(m^t) + N_{\text{bkg}} B(m^t), \quad (2)$$

which contains the distributions  $T(m^t)$  and  $B(m^t)$  of the signal and the subdominant backgrounds, respectively, taken from the simulation, and the distribution  $Q(m^t)$  of the QCD multijet background, taken from the control sample in data. To account for a possible difference in the QCD multijet  $m^t$  distribution between the control and signal regions, a linear modification factor  $(1 + k_{\text{slope}} m^t)$  is introduced, inspired by the simulation, but with the slope parameter  $k_{\text{slope}}$  left free in the fit. Also free in the fit are the normalization factors  $N_{\text{tt}}$ ,  $N_{\text{QCD}}$ , and  $N_{\text{bkg}}$ . Two additional nuisance parameters are introduced in the simulated  $t\bar{t}$  distribution,  $k_{\text{scale}}$  and  $k_{\text{res}}$ , which account for possible differences between data and simulation in the scale and resolution of the  $m^t$  parameter. The fit is performed with the ROOFIT toolkit [52] and the fit results are shown in Fig. 1 and Table 1. The fitted  $t\bar{t}$  yield is significantly lower than the expectation (9885), which implies that the fiducial cross section is lower compared to the POWHEG+PYTHIA prediction with a post-fit signal strength of  $0.64 \pm 0.03$ . This value is used to scale down the expected  $t\bar{t}$  signal yields from the POWHEG+PYTHIA simulation in the various signal regions in the subsequent figures with data vs simulation comparisons. The nuisance parameters that control the scale and the resolution of the reconstructed mass are consistent with one, confirming the excellent agreement between data and simulation of this variable.

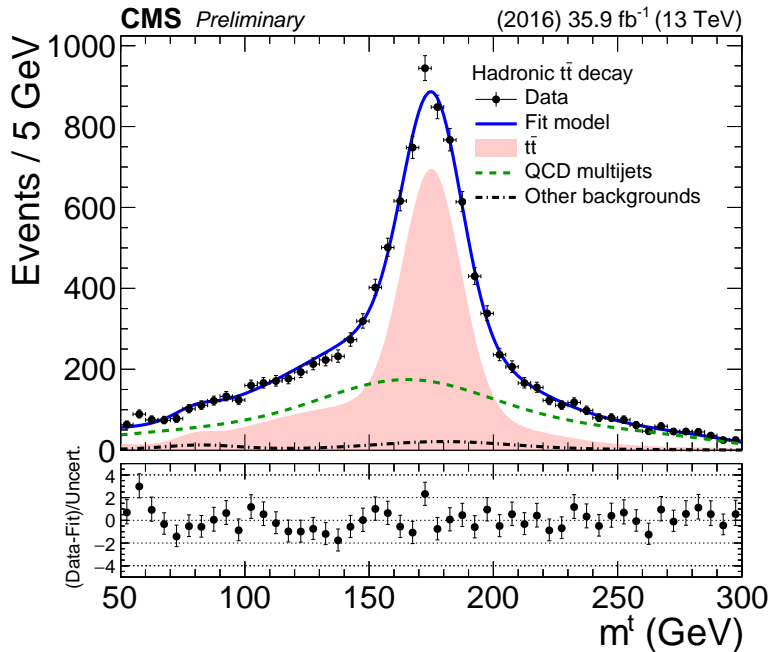


Figure 1: Result of the fit to data of the soft-drop mass of the  $t$  jet candidate,  $m^t$ , in  $\text{SR}_A$  for the hadronic channel. The shaded area shows the  $t\bar{t}$  contribution, the dashed line shows the QCD multijet background, and the double-dashed line shows the other subdominant backgrounds. The solid line shows the combined signal plus background fit model, and the data points are shown with solid markers. The bottom panel shows the data minus the fit model, divided by the fit uncertainty.

The subdominant background processes, namely single top quark production and vector bosons produced in association with jets, have a negligible contribution in the signal region (below 1% in the entire phase space) and are fixed to the predictions from simulation.

Figure 2 shows the distribution of the NN output in  $\text{SR}_B$  and Figs. 3, 4 show the kinematic

Table 1: Post-fit values of the nuisance parameters for the fit to data in  $\text{SR}_A$  in the hadronic channel.

Parameter	Value
$k_{\text{res}}$	$0.960 \pm 0.026$
$k_{\text{scale}}$	$1.002 \pm 0.002$
$k_{\text{slope}}$	$(5.7 \pm 1.4) \times 10^{-3}$
$N_{\text{bkg}}$	$400 \pm 255$
$N_{\text{QCD}}$	$4539 \pm 247$
$N_{t\bar{t}}$	$6238 \pm 181$

properties of the two top quark candidates and the  $t\bar{t}$  system, respectively. Also, the soft-drop masses of the two jets are shown in Fig. 5. In these figures, the  $t\bar{t}$  and QCD multijet processes are normalized according to the results of the fit in  $\text{SR}_A$  described above, while the yields of the subdominant backgrounds are taken from the simulation. Table 2 summarizes the event yields in the SR.

Table 2: Observed and predicted event yields with their respective statistical uncertainties in the signal region for the hadronic channel. The  $t\bar{t}$  and QCD multijet yields are obtained after the fit in  $\text{SR}_A$ .

Process	Number of events
$t\bar{t}$	$4244 \pm 127$
QCD multijets	$1876 \pm 102$
Single t	$83 \pm 41$
W+jets	$58 \pm 29$
Z+jets	$12 \pm 6$
Total	$6273 \pm 171$
Data	6274

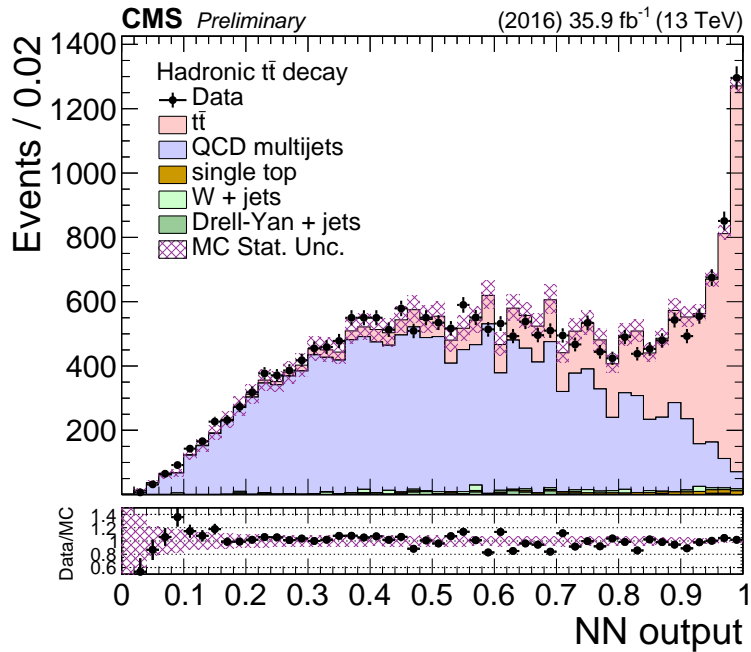


Figure 2: Comparison between data and simulation in  $\text{SR}_B$  (same as the SR, without any NN requirement) of the NN output in the hadronic channel. The  $t\bar{t}$  and QCD multijet processes are normalized according to the post-fit values of the respective yields and are shown as stacked histograms. The data points are shown with solid markers, while the shaded band represents the statistical uncertainty in the simulation. The bottom panel shows the data divided by the sum of the prediction from the simulation.

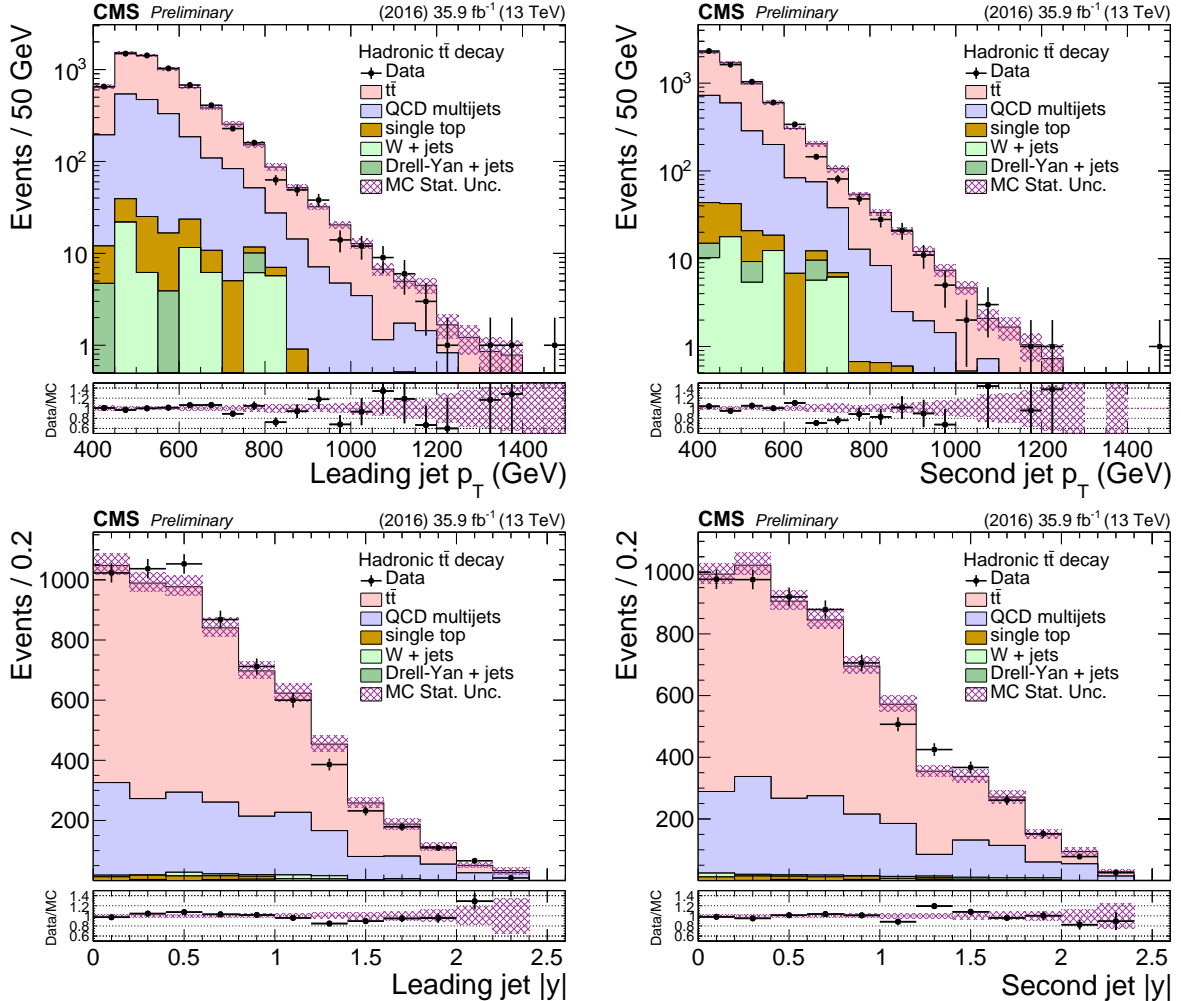


Figure 3: Comparison between data and simulation in the signal region of the  $p_T$  (top row) and absolute rapidity (bottom row) of the leading (left column) and subleading (right column) large- $R$  jets in the hadronic channel. The  $t\bar{t}$  and QCD multijet processes are normalized according to the post-fit values of the respective yields and are shown as stacked histograms. The data points are shown with solid markers, while the shaded band represents the statistical uncertainty in the simulation. The bottom panel shows the data divided by the sum of the prediction from the simulation.

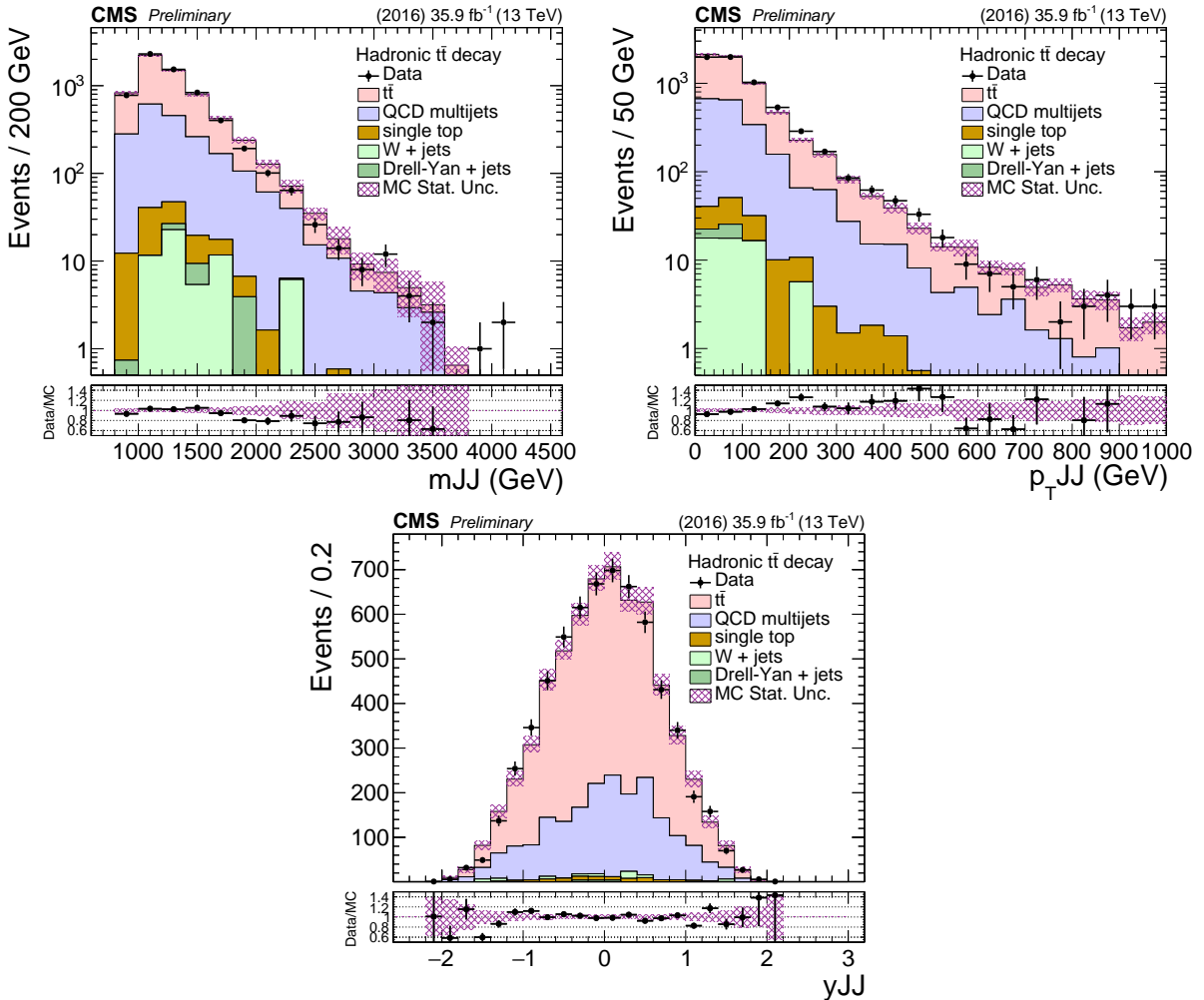


Figure 4: Comparison between data and simulation in the signal region in the hadronic channel of the  $t\bar{t}$  system variables reconstructed from the two leading large- $R$  jets, specifically, the invariant mass (top left),  $p_T$  (top right), and rapidity (bottom). The  $t\bar{t}$  and QCD multijet processes are normalized according to the post-fit values of the respective yields and are shown as stacked histograms. The data points are shown with solid markers, while the shaded band represents the statistical uncertainty in the simulation. The bottom panel shows the data divided by the sum of the prediction from the simulation.

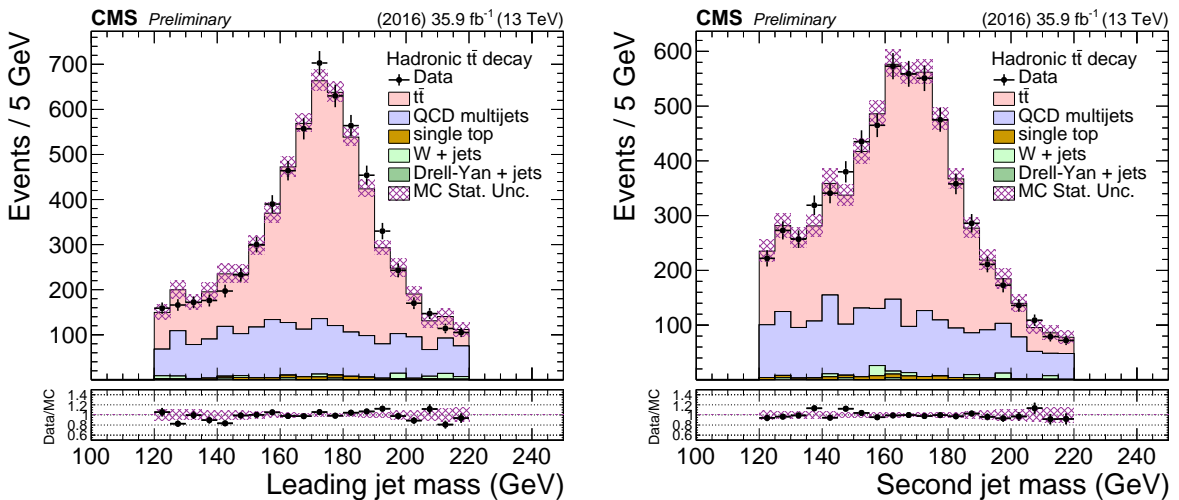


Figure 5: Comparison between data and simulation in the signal region of the mass of the leading (left) and subleading (right) large- $R$  jets in the hadronic channel. The  $t\bar{t}$  and QCD multijet processes are normalized according to the post-fit values of the respective yields and are shown as stacked histograms. The data points are shown with solid markers, while the shaded band represents the statistical uncertainty in the simulation. The bottom panel shows the data divided by the sum of the prediction from the simulation.

In the  $\ell$ +jets channel, background events due to non-signal  $t\bar{t}$ , single top quark,  $W/Z$ +jets, and diboson production are estimated from simulation. The QCD multijet background is modeled with data-based techniques, using a data sideband region that is defined by inverting the isolation requirement on the lepton and relaxing the lepton identification criteria. The predicted contributions to the sideband region from signal and other background events are subtracted from the observed data distribution in the sideband region to yield the kinematic distributions for QCD multijet events. The normalization of the QCD multijet background is extracted from a maximum likelihood fit, described in Section 6.2; an initial estimate of its normalization is taken as the simulated prediction in the signal region. The normalizations of the other background processes are also constrained through the fit.

$$QCD\_sideband(x) = D\_sideband(x) - S\_sideband(x) - Bkg\_sideband(x)$$

## 6 Signal extraction

### 6.1 Hadronic channel

In the hadronic channel, the  $t\bar{t}$  signal is extracted from data by subtracting the contribution from the background processes. The signal extraction is performed differentially, as a function of seven variables:  $p_T$  and absolute rapidity  $|y|$  of the leading and subleading  $t$  jet, as well as the mass,  $p_T$ , and  $y$  of the  $t\bar{t}$  system. That is:

$$S(x) = D(x) - R_{yield} N_{QCD} Q(x) - B(x), \quad (3)$$

where  $x = p_T^{t1,2}, |y^{t1,2}|, m^{t\bar{t}}, p_T^{t\bar{t}}$ , or  $y^{t\bar{t}}$ ,  $S(x)$  is the  $t\bar{t}$  signal,  $D(x)$  is the measured distribution in data,  $Q(x)$  is the QCD multijet distribution, and  $B(x)$  is the contribution from the subdominant backgrounds (for which both the distribution and the normalization are taken from the simulation). These quantities are taken from the signal region. The variable  $N_{QCD}$  is the fitted number of QCD multijet events in  $SR_A$  and the factor  $R_{yield}$  is found (in simulation) to be independent of the  $b$  tagging requirement and therefore it is estimated from the QCD multijet control data sample as  $R_{yield} = N_{QCD}^{SR}/N_{QCD}^{SR_A} = N_{QCD}^{CR}/N_{QCD}^{CR_A} \approx 0.38 \pm 0.02$ .

### 6.2 Lepton+jets channel

For the analysis in the  $\ell$ +jets channel, the  $t\bar{t}$  signal strength,  $t$  tagging efficiency scale factor, and background normalizations are determined in a simultaneous binned maximum likelihood fit to the data across the different analysis event categories.

The 0t, 1t0b, and 1t1b event categories are fitted simultaneously, normalizing each background component to the same cross section in all categories. The fit result is expressed in terms of a multiplicative factor, the signal strength  $r$ , applied to the input  $t\bar{t}$  cross section. Different variables are used to discriminate the  $t\bar{t}$  signal from the background processes. The small- $R$  jet  $\eta$  distribution is used in the 0t and 1t0b categories, while the large- $R$  jet soft-drop mass distribution is used in the 1t1b region. These distributions were chosen to have good discrimination between  $t\bar{t}$ ,  $W$ +jets, and QCD multijet production, as  $t\bar{t}$  events tend to be produced more centrally than the background and the soft-drop mass distribution peaks around the top quark mass for signal events. The  $t\bar{t}$  signal and  $t\bar{t}$  background distributions are merged into a single distribution for the purpose of the fit, essentially constraining the semileptonic branching fraction to be equal to that provided by the simulation.

Background normalizations and experimental sources of systematic uncertainty are treated as nuisance parameters in the fit. The uncertainties due to pileup reweighting, lepton scale fac-

tors, jet energy scale and resolution, b tagging efficiency, and t tagging efficiency are treated as uncertainties in the shape of the input templates. Two separate nuisance parameters are used to describe the t tagging uncertainty: one for the t tagging scale factor that is applied to the  $t\bar{t}$  and single top quark ( $tW$ ) samples, where we expect the t-tagged jet to correspond to a true top quark decay, while the t mistag scale factor is applied for the remaining background samples. The uncertainties in the luminosity and background normalizations are treated as rate uncertainties. The event categories that are fitted are designed such that the t tagging efficiency is constrained by the relative population of events in the three categories. The varying admixtures of signal and background between the different event categories allows constraining the background normalizations. The measurement of the signal strength is correlated with the various nuisance parameters, with the strongest correlation being with the t tagging efficiency, as expected. For the shape uncertainties, the nuisance parameter is used to interpolate between the nominal kinematic distribution and distributions corresponding to  $\pm 1$  standard deviation ( $\sigma$ ) variations in the given uncertainty. The uncertainties due to the theoretical modeling are evaluated independently from the fit.

The  $e/\mu+jets$  channels are fitted simultaneously, with most nuisance parameters constrained to be the same in both channels. The nuisance parameters associated with the electron and muon scale factors are treated separately, as are the electron and muon QCD multijet background normalizations. The posterior kinematic distributions for the three event categories are shown in Fig. 6. The event counts that account for all posterior parameters are given in Table 3.

Process	Number of events ( $\mu+jets$ channel)		
	0t	1t0b	1t1b
$t\bar{t}$	$16772 \pm 1438$	$4245 \pm 174$	$3905 \pm 80$
Single t	$3286 \pm 587$	$282 \pm 68$	$153 \pm 34$
W+jets	$23104 \pm 2871$	$2368 \pm 318$	$105 \pm 20$
Z+jets	$2582 \pm 680$	$234 \pm 69$	$19 \pm 10$
Diboson	$557 \pm 155$	$31 \pm 10$	$2 \pm 1$
QCD multijets	$2833 \pm 1207$	$159 \pm 76$	$43 \pm 22$
Total	$49135 \pm 3549$	$7320 \pm 383$	$4228 \pm 93$
Data	49137	7348	4187

Process	Number of events ( $e+jets$ channel)		
	0t	1t0b	1t1b
$t\bar{t}$	$10707 \pm 938$	$2835 \pm 116$	$2670 \pm 66$
Single t	$2267 \pm 403$	$191 \pm 47$	$107 \pm 24$
W+jets	$13945 \pm 1742$	$1445 \pm 194$	$62 \pm 12$
Z+jets	$1068 \pm 295$	$118 \pm 37$	$17 \pm 15$
Diboson	$373 \pm 105$	$22 \pm 7$	$2 \pm 1$
QCD multijets	$3200 \pm 735$	$242 \pm 80$	$31 \pm 30$
Total	$31560 \pm 2171$	$4854 \pm 247$	$2889 \pm 79$
Data	31559	4801	2953

Table 3: Posterior signal and background event yields in the 0t, 1t0b, and 1t1b categories, together with the observation in data. The uncertainties include all posterior experimental uncertainties.

Figure 7 shows the  $p_T$  and  $y$  distributions for the t jet candidate in each of the three event categories for the combined  $\ell+jets$  channel. These distributions use the posterior t tagging scale

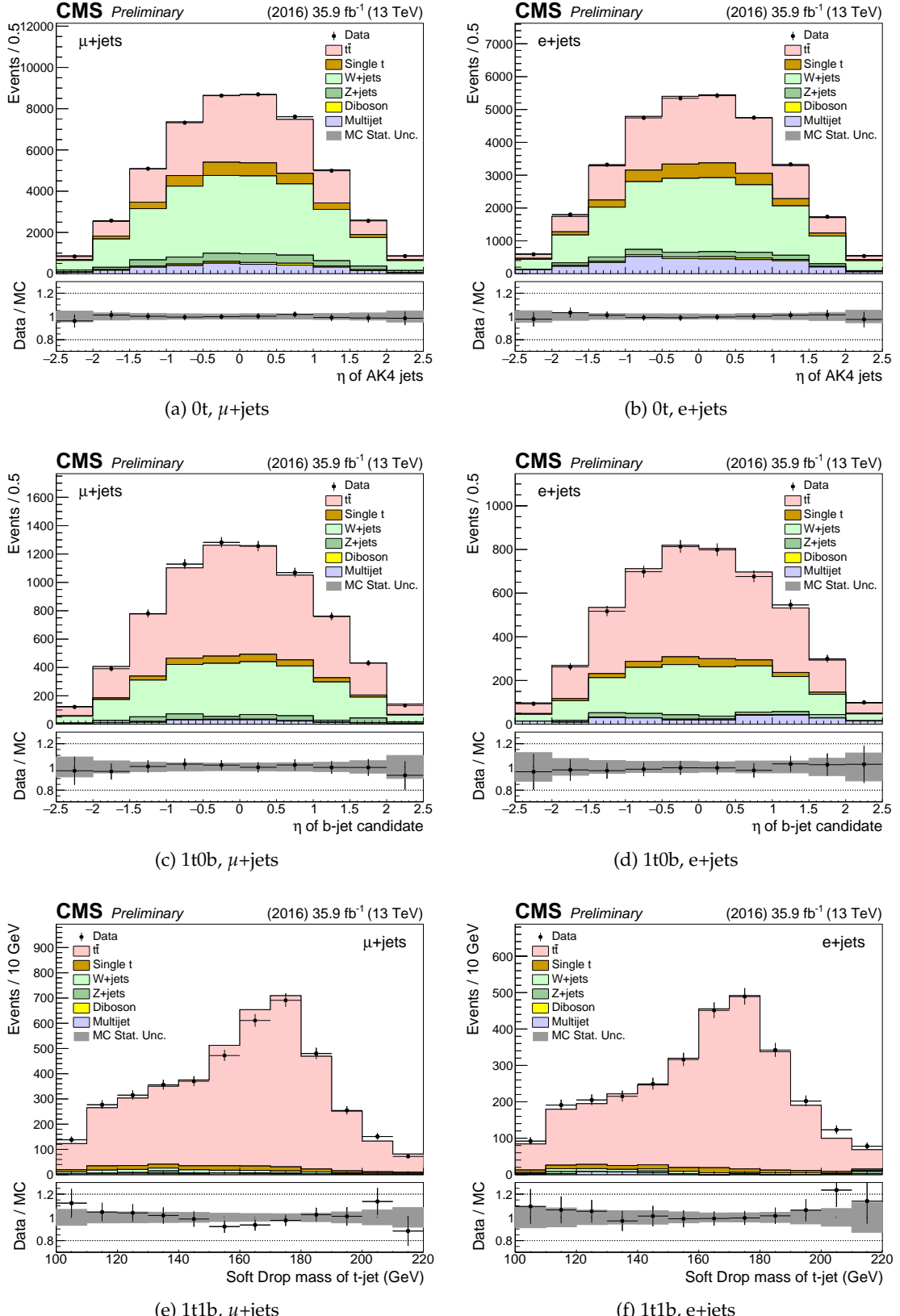


Figure 6: Posterior kinematic distributions for the maximum likelihood fit. Different event categories and variables are used:  $\eta$  distribution for the small- $R$  jet in 0t events (top),  $\eta$  distribution of the b jet candidate in 1t0b events (middle), and soft drop mass of the t jet candidate in 1t1b events (bottom), in the  $\mu$ +jets (left) and  $e$ +jets (right) channels. The data points are shown with solid markers, while the signal and background predictions are shown as stacked histograms. The bottom panel shows the data divided by the sum of the prediction from the simulation (solid markers) and the systematic uncertainty from the fit (shaded band).

factor and background normalizations, but not the posterior values of other nuisance parameters. The posterior  $t$  tagging efficiency (misidentification) scale factor is  $1.04 \pm 0.06$  ( $0.79 \pm 0.06$ ), with an additional  $t$  jet  $p_T$  and  $\eta$  dependent uncertainty in the range 1–8% (1–13%). The post-fit background normalizations are generally in good agreement with their corresponding pre-fit values, only the  $W$ +light jet normalization is low by about  $1\sigma$ .

The posterior signal strength as determined in the fit is  $0.81 \pm 0.05$ , i.e. the  $t\bar{t}$  simulation is observed to overestimate the data by roughly 25% in the fiducial phase space region. Although the measured signal strength extrapolated from the fit is not directly used in measuring the differential cross section, it serves as an indicator of the level of agreement between the measured integrated  $t\bar{t}$  cross section and the prediction from the simulation in the boosted regime.

## 7 Systematic uncertainties

The systematic uncertainties considered in this measurement originate from both experimental and theoretical sources. The former include all uncertainties related to the differences in the particle reconstruction and identification performance between data and simulation, as well as the background modeling. The latter are related to the  $t\bar{t}$  signal simulation and affect primarily the unfolded results through the acceptance, efficiency, and migration matrices. For each systematic variation, the differential cross section measurement is repeated and the difference with respect to the nominal result is taken as the effect of this variation on the measurement.

A number of experimental uncertainties affect the measurement. The dominant sources of systematic uncertainty in the hadronic channel are due to the jet energy scale and the  $b$  tagging efficiency. In the  $\ell+jets$  channel, the  $t$  tagging and  $b$  tagging efficiency uncertainties result in the largest contributions. The different sources are described in detail in the list below:

- ***QCD multijet background (hadronic)***: The fitted QCD multijet yield uncertainty is used, as well as the uncertainty in  $R_{yield}$  (Eq. 3). The impact of the shape uncertainties, estimated by comparing the distribution of each variable between the signal region SR and the control region CR (see Section 4) in simulated events, as well as the different pileup profiles for data collected with the control trigger compared to the signal trigger, are of the order of 1%. The uncertainty in  $R_{yield}$  is dominated by the uncertainty of the method (estimated with simulated events), while there is a smaller statistical contribution.
- ***Subdominant backgrounds (hadronic)***: The expected yield of the subdominant background processes estimated from the simulation (single top quark production and vector bosons produced in association with jets) is varied by  $\pm 50\%$ , leading to a negligible uncertainty (smaller than 1%).
- ***Background estimate ( $\ell+jets$ )***: An a priori uncertainty of 30% is applied to the single top quark and  $W+jets$  background normalizations. An additional uncertainty in the flavor composition of the  $W+jets$  process is considered, allowing the light- and heavy-flavor components to vary independently with a 30% normalization uncertainty. For the QCD multijet normalization, an a priori uncertainty of 50% is used to reflect the combined uncertainty in the normalization and the extraction of the kinematic distributions from the data sideband region. These are all constrained in the maximum likelihood fit.
- ***Jet energy scale***: The uncertainty in the energy scale of each reconstructed large- $R$  jet, referred to as the jet energy scale (JES) uncertainty, is a leading experimental uncertainty in the hadronic channel. It is divided in 24 independent sources [42]

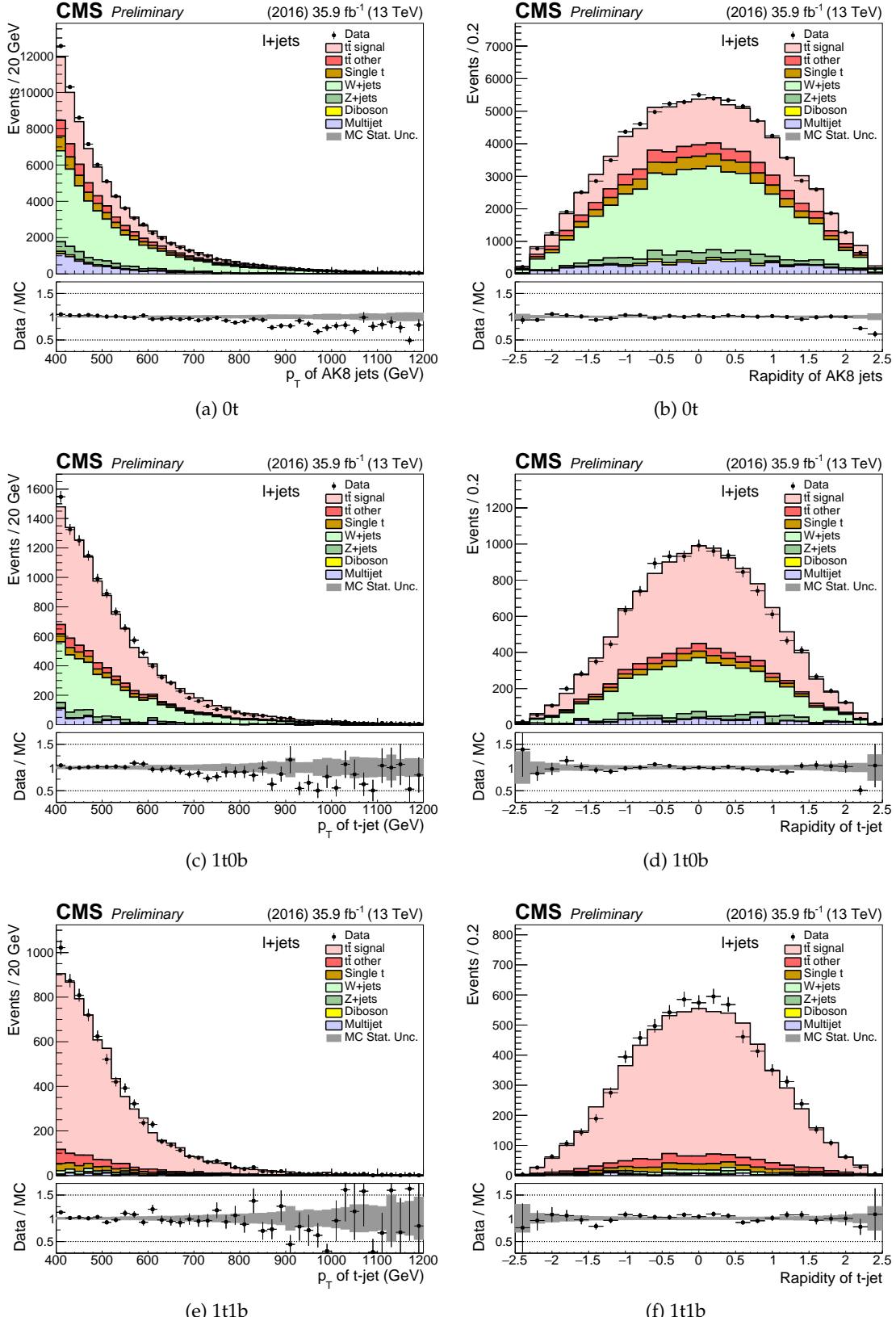


Figure 7: Distributions of the  $p_T$  (left) and  $y$  (right) of the  $t$  jet candidate for the 0t (top), 1t0b (middle), and 1t1b (bottom) regions for events in the combined  $\ell + \text{jets}$  channel. The posterior  $t$  tag scale factor and background normalizations are used. The data points are shown with solid markers, while the signal and background predictions are shown as stacked histograms. The bottom panel shows the data divided by the sum of the prediction from the simulation (solid markers) and the systematic uncertainty from the fit (shaded band).

and treated as follows: for each variation a new jet collection is created and the event interpretation is repeated. This results not only in variations of the  $p_T$  scale itself, but may also lead to different t jet candidates. The  $p_T$  and  $\eta$  dependent JES uncertainty is of the order of 1–2% per jet. The resulting uncertainty in the measured cross section is typically of the order of 10% but it can be much larger at high top quark  $p_T$ . For the  $\ell$ +jets channel, the jet energy scale uncertainty is estimated for both small- $R$  and large- $R$  jets by shifting the jet energy in simulation up or down by their  $p_T$  and  $\eta$  dependent uncertainties, with a resulting impact on the differential cross section measurements of 1–10%.

- **Jet energy resolution:** The impact on the measurement due to the jet energy resolution (JER) is determined by smearing the jets according to the JER uncertainty [42]. The effect on the cross section is relatively small, at the level of 2%.
- **t tagging efficiency ( $\ell$ +jets):** The t tagging efficiency and its associated uncertainty is simultaneously extracted with the signal strength and background normalizations in the likelihood fit for the  $\ell$ +jets analysis, described in Section 6. The uncertainty in the t tagging efficiency is in the range 6–10%, while for the misidentification rate it is 8–15%, depending on t jet  $p_T$  and  $\eta$ .
- **Subjet b tagging efficiency (hadronic):** The uncertainty in the identification of b subjets within the large- $R$  jets (estimated in [51]) is a leading experimental uncertainty in the hadronic channel. The effect on the cross sections is of the order of 10%, relatively flat in all the observables. Unlike the uncertainty associated with the JES, the b-subjet tagging uncertainty therefore largely cancels in the normalized cross sections.
- **b tagging efficiency ( $\ell$ +jets):** For the  $\ell$ +jets channel, the small- $R$  jet b tagging efficiency in the simulation is corrected to match that measured in data using  $p_T$ - and  $\eta$ -dependent scale factors [51]. The resulting uncertainty in the differential cross sections is about 1–2%. The b tagging efficiency and light jet misidentification uncertainties are treated as fully correlated.
- **Pileup:** The uncertainty related to the modeling of additional pileup interactions is a subdominant uncertainty. The impact on the measurement is estimated by varying the total inelastic cross section used to weight the simulated events by  $\pm 4.6\%$  [53]. The effect on the cross sections is negligible (below 1%).
- **Trigger (hadronic):** The uncertainty associated with the trigger, accounting for the difference between the simulated and observed trigger efficiency, is well below 1% in the phase space of the hadronic channel.
- **Lepton identification and trigger ( $\ell$ +jets):** The performance of the lepton identification, reconstruction, trigger, and isolation constitutes a small source of systematic uncertainty. Correction factors used to modify the simulation to match the efficiencies observed in data are estimated with a tag-and-probe method using  $Z \rightarrow \ell\ell$  decays. The corresponding uncertainty is determined by varying the correction factors up or down within their uncertainties. The resulting systematic uncertainties depend on lepton  $p_T$  and  $\eta$ , and are in the range 1–7% and 1–5% for electrons and muons, respectively.
- **Luminosity:** The uncertainty in the measurement of the integrated luminosity is 2.5% [54].

The theoretical uncertainties are divided into two sub-categories: sources of systematic uncertainty related to the matrix element of the hard scatter process and sources related to the modeling of the parton shower and the underlying event. The first category (consisting of the

first three sources below) is evaluated using variations of the simulated event weights, while the second category is evaluated with dedicated, alternative MC samples with modified parameters. These sources are:

- *Parton distribution functions*: The uncertainty due to PDFs is estimated by applying event weights corresponding to the 100 replicas of the NNPDF set [30]. For each observable we compute its standard deviation from the 100 variations.
- *Renormalization and factorization scales*: This source of systematic uncertainty is estimated by applying event weights corresponding to different factorization and renormalization scale options. Both scales are varied independently by a factor of two up or down in the event generation, omitting the two cases where the scales are varied in opposite directions, and taking the envelope of the six resulting variations.
- *Strong coupling constant ( $\alpha_S$ )*: The uncertainty associated with the  $\alpha_S$  is estimated by applying event weights corresponding to higher or lower values of  $\alpha_S$  for the matrix element using the variations of the NNPDF set [30].
- *Initial- and final-state radiation*: The uncertainty in the initial-state radiation (ISR) and the final-state radiation (FSR) is estimated from alternative MC samples with reduced or increased values for the strong coupling constant used by PYTHIA to generate initial- or final-state radiation. The scale in the ISR is varied by factors of 2 and 0.5, and the scale in the FSR by factors of  $\sqrt{2}$  and  $1/\sqrt{2}$  [55]. In the hadronic channel, the FSR uncertainty is constrained by a fit to the data in the signal region  $SR_B$ , using the NN output that is sensitive to the modelling of the FSR. This leads to a reduction by a factor 0.3 relative to the variations from the alternative MC samples.
- *Matrix element – parton shower matching*: In the POWHEG matrix element to parton shower (ME-PS) matching scheme, the resummation damping factor  $h_{\text{damp}}$  is used to regulate high- $p_T$  radiation. The nominal value is  $h_{\text{damp}} = 1.58m_t$ , with  $m_t$  being the generated top quark mass. Uncertainties in  $h_{\text{damp}}$  are parameterized by considering alternative simulated samples with  $h_{\text{damp}} = m_t$  and  $h_{\text{damp}} = 2.24m_t$ .
- *Underlying event tune*: This uncertainty is estimated from alternative MC samples with the tune CUETP8M2T4 parameters varied by  $\pm 1\sigma$ .

## 8 Cross section measurements

This section discusses the differential  $t\bar{t}$  production cross section measurements for the hadronic and  $\ell + \text{jets}$  channels. The cross sections are measured as a function of different kinematic variables for the top quark or the  $t\bar{t}$  system, and are corrected to the particle and parton level using an unfolding procedure. The measurements are compared to predictions from different MC event generators and high-order calculations.

### 8.1 Definition of the particle and parton level

The parton-level phase space to which the measurement is unfolded is constrained by the kinematic requirements of the detector-level fiducial region. Namely, for the hadronic channel, the top quark and antiquark must have  $p_T > 400 \text{ GeV}$  and  $|\eta| < 2.4$ , while the invariant mass of the  $t\bar{t}$  system must be greater than  $800 \text{ GeV}$  in order to avoid extreme events with high top quark  $p_T$  and very low  $m_{t\bar{t}}$ .

The parton-level definition for the  $\ell + \text{jets}$  channel differs from the hadronic channel because the differential cross section is reported as a function of the hadronically decaying top quark.

Therefore, the parton-level phase space is confined to semileptonic events, where the  $p_T$  of the hadronically decaying top quark is greater than 400 GeV, to match the fiducial requirement at the detector level.

The so-called *particle level* represents the state that consists of stable particles originating from the  $pp$  collision, after the hadronization process but before the interaction of these particles with the detector. The observables computed from the particles' momenta are thought to be better defined compared to the ones computed from parton-level information. Also, the associated phase space is closer to the fiducial phase space of the measurement at the detector level, which results in smaller theoretical uncertainties. In the context of this analysis, particle jets are reconstructed from stable particles, excluding neutrinos, with the anti- $k_T$  algorithm using a distance parameter of 0.8, identical to the detector-level reconstruction. Only particles originating from the primary interaction are considered. Subsequently, jets that are geometrically matched, within  $\Delta R < 0.4$  in  $\eta - \phi$ , to generated leptons (i.e. from the leptonic decays of W bosons) are removed from the particle jet collection. For the hadronic channel, the two particle jets with the highest  $p_T$  are considered the particle-level t candidates. In order to match as closely as possible the fiducial phase space, the same kinematic selection criteria are applied as for the detector-level events. In particular, the particle-level jets must have  $p_T > 400$  GeV and  $|\eta| < 2.4$ , while the mass of each jet should be in the range 120–220 GeV and the invariant mass of the two jets be greater than 800 GeV. The matching efficiency between the particle-level t candidates and the original top quarks at the parton level varies between 96% and 98%.

The particle-level phase space for the  $\ell+jets$  channel is set up to mimic the kinematic selections at the detector level. Particle-level large- $R$  jets are selected if they fulfill  $p_T > 400$  GeV,  $|\eta| < 2.4$ , and  $105 < m_{jet} < 220$  GeV, and are then referred to as particle-level t jets. Particle-level small- $R$  jets are selected if they have  $p_T > 50$  GeV,  $|\eta| < 2.4$ , and are flagged as a b jet; these are referred to as particle-level b jets. Particle-level electrons and muons are selected if they have  $p_T > 50$  GeV and  $|\eta| < 2.1$ . To fulfill the particle-level selection criteria, an event must contain at least one particle-level t jet, at least one particle-level b jet, and at least one particle-level electron or muon.

In order to quantify the overlap between the detector-, particle-, and parton-level phase space definitions, two fractions,  $f_{1,2}$ , are used. Here  $f_1$  is defined as the fraction of reconstructed events that are accompanied by a selected event at the unfolded level (parton or particle) in the same observable range, whereas  $f_2$  is the fraction of events at the unfolded level that is accompanied by a selected reconstructed event. Figures 8 and 9 show the aforementioned fractions at the parton and particle level, respectively, for the hadronic channel as a function of the leading top quark  $p_T$  and  $|y|$ . The  $f_1$  vs  $p_T$  shows a characteristic threshold behavior due to the finite  $p_T$  resolution, while it is flat vs  $|y|$ . The  $f_2$  decreases vs  $p_T$ , primarily due to the subjet b tagging inefficiency and the NN output dependence on the  $p_T$  (at high jet  $p_T$  it is more difficult to differentiate between ordinary QCD jets and boosted top quarks). Also, the  $f_2$  decreases at high  $|y|$  values due to the increased b tagging inefficiency at the edges of the CMS tracker detector.

## 8.2 Unfolding

To extract the differential cross sections at the particle and parton level, an unfolding method is applied. Specifically, the unfolded differential cross sections are extracted according to

$$\frac{d\sigma_i^{\text{unf}}}{dx} = \frac{1}{\mathcal{L} \cdot \Delta x_i} \cdot \frac{1}{f_{2,i}} \cdot \sum_j \left( R_{ij}^{-1} \cdot f_{1,j} \cdot S_j \right), \quad (4)$$

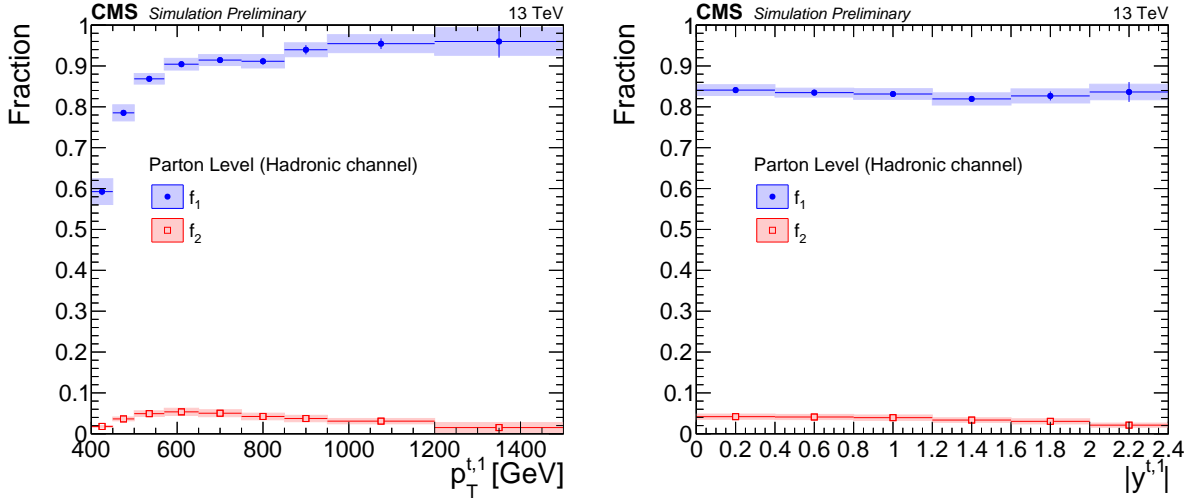


Figure 8: Simulated fractions  $f_{1,2}$  for the parton-level selection in the hadronic channel as a function of the leading top quark  $p_T$  (left) and  $|y|$  (right).

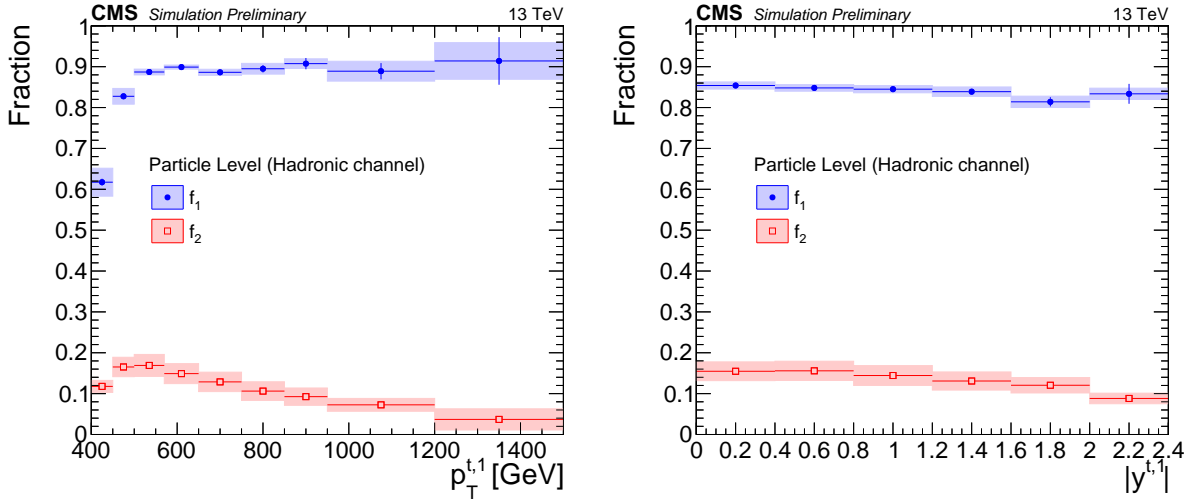


Figure 9: Simulated fractions  $f_{1,2}$  for the particle-level selection in the hadronic channel as a function of the leading top quark  $p_T$  (left) and  $|y|$  (right).

where  $\mathcal{L}$  is the total integrated luminosity and  $\Delta x_i$  is the width of the  $i$ -th bin of the observable  $x$ . The quantity  $R_{ij}^{-1}$  is the inverse of the migration matrix between the  $i$ -th and  $j$ -th bins. Due to the finite resolution of the detector, the migration matrix is non-diagonal and thus the application of an unfolding procedure is necessary. The binning of the various observables has been chosen such that the purity (fraction of reconstructed events for which the true value of the observable lies in the same bin) and the stability (fraction of true events where the reconstructed observable lies in the same bin) are well above 50%. This choice results in migration matrices with suppressed non-diagonal elements, shown for the hadronic channel in Figs. 10 and 11, and for the  $\ell+jets$  channel in Figs. 12 and 13. In order to avoid the biases introduced by the various unfolding methods utilizing some type of regularization, the simple migration matrix inversion is used, as written in Eq. 4, at a price of a moderate increase in the statistical uncertainty.

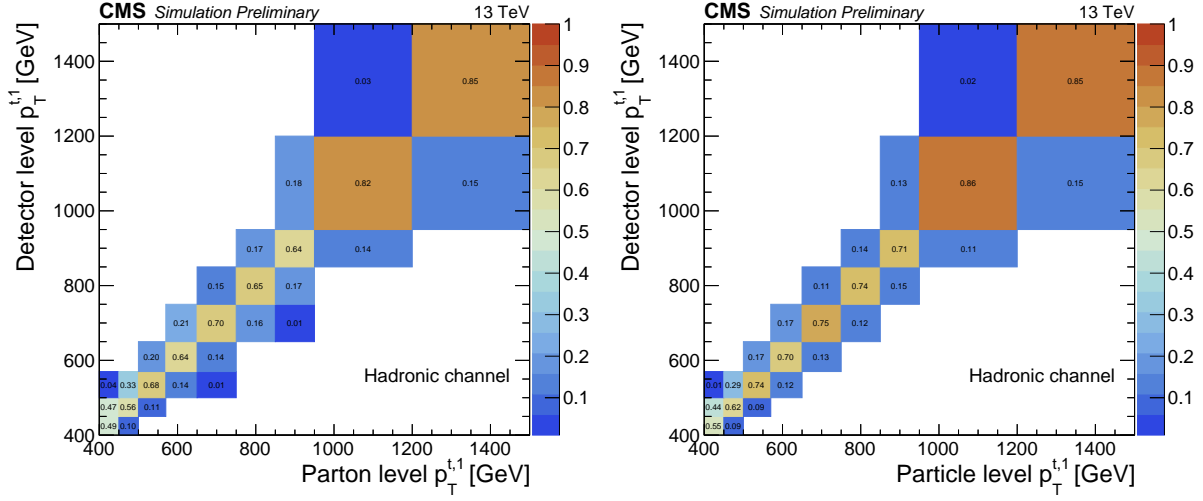


Figure 10: Simulated migration matrices for the leading top quark  $p_T$  at the parton level (left) and particle level (right) in the hadronic channel. Each column is normalized to unity.

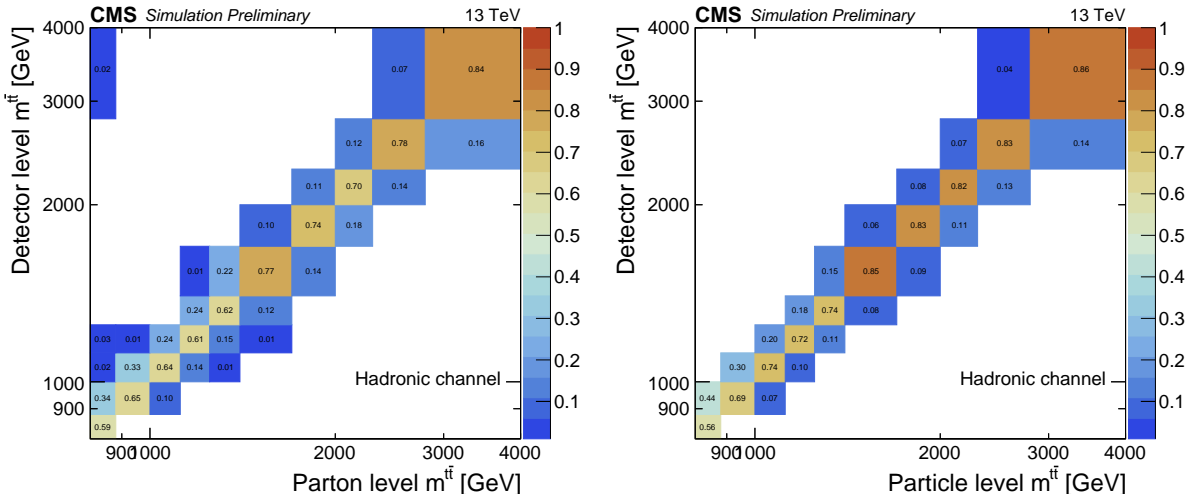


Figure 11: Simulated migration matrices for  $m_{t\bar{t}}$  at the parton level (left) and particle level (right) in the hadronic channel. Each column is normalized to unity.

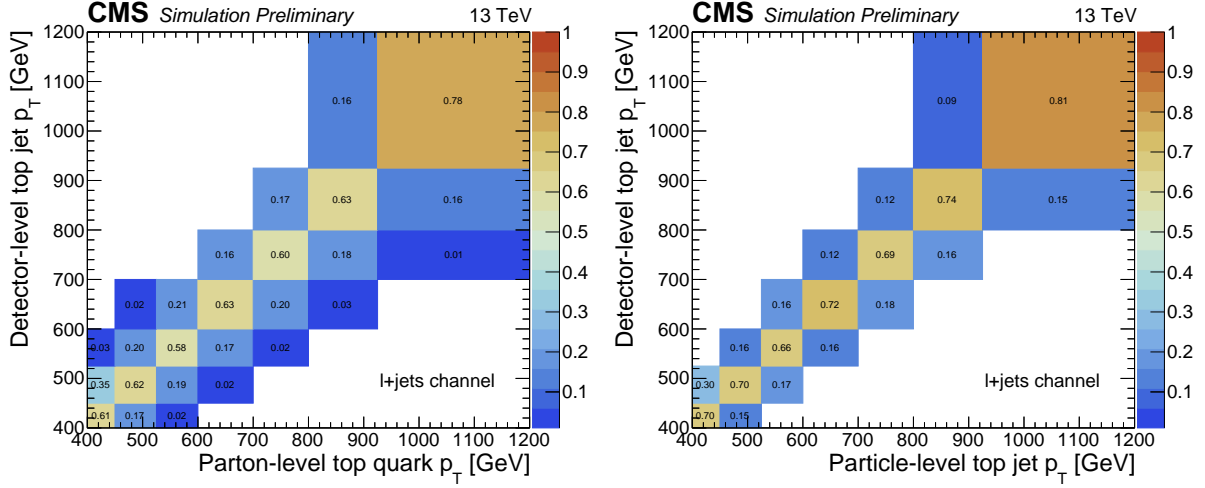


Figure 12: Simulated migration matrices for top quark  $p_T$  at the parton level (left) and particle level (right) in the  $\ell$ +jets channel. Each column is normalized to unity.

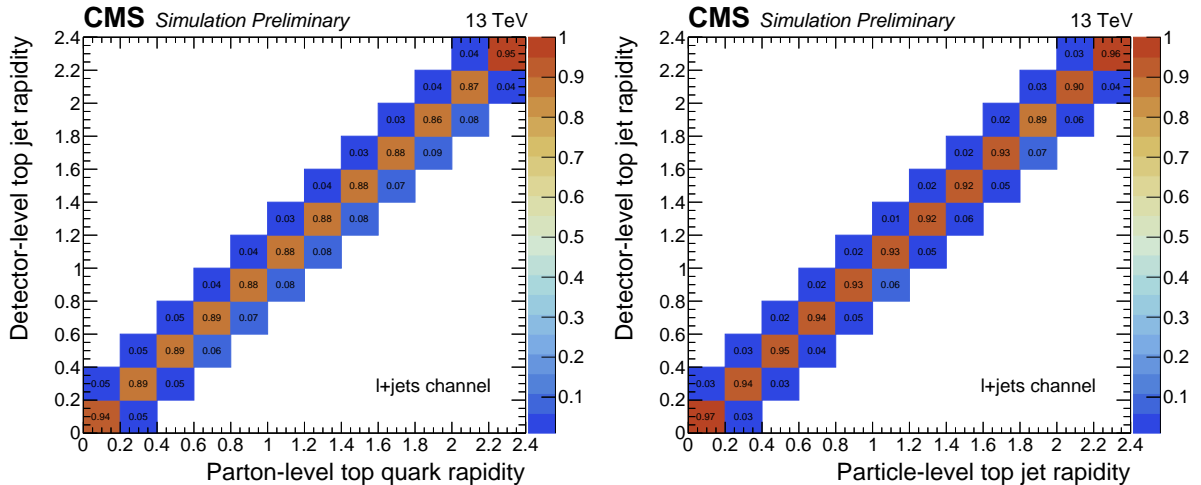


Figure 13: Simulated migration matrices for top quark rapidity at the parton level (left) and particle level (right) in the  $\ell$ +jets channel. Each column is normalized to unity.

### 8.3 Hadronic channel

For the hadronic channel, the measurement of the unfolded differential cross section in bin  $i$  of the variable  $x$  is performed using Eq. 4, where the signal yield  $S_i$  is computed from Eq. 3. In order to estimate the uncertainty in the measurement, the entire procedure of the signal extraction, unfolding with different response matrices, and extrapolation to the particle- or parton-level phase space is repeated for every source of uncertainty discussed in Section 7. The unfolded cross sections at the particle level are shown in Figs. 14–20 and at the parton level in Figs. 21–27. Figures 28 and 29 show a summary of the statistical and the dominant systematic uncertainties in the differential cross section measurements as a function of the leading top quark  $p_T$  and  $|y|$  at the particle and parton level, respectively.

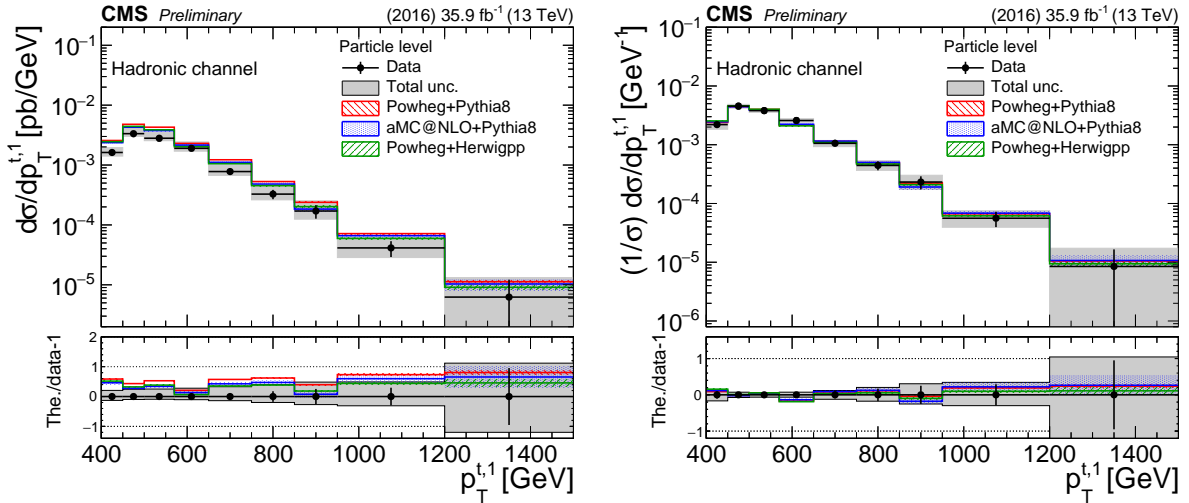


Figure 14: Differential cross section unfolded to the particle level, absolute (left) and normalized (right), as a function of the leading top quark  $p_T$  in the hadronic channel. The bottom panel shows the ratio  $(\text{theory} - \text{data})/\text{data}$ . The uncertainties on the data markers are statistical, while the grey band shows the total statistical and systematic uncertainty.

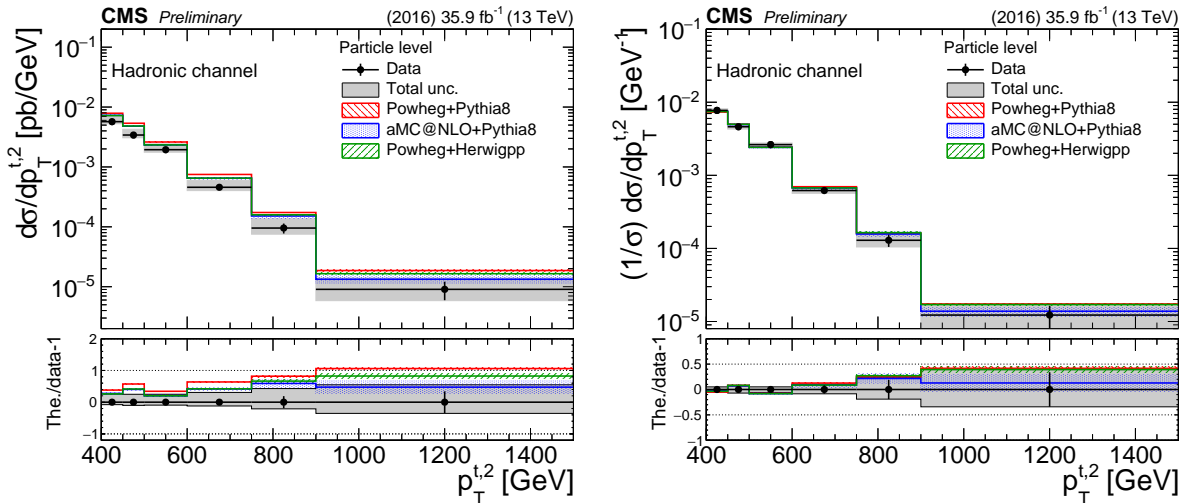


Figure 15: Differential cross section unfolded to the particle level, absolute (left) and normalized (right), as a function of the second top quark  $p_T$  in the hadronic channel. The bottom panel shows the ratio  $(\text{theory} - \text{data})/\text{data}$ . The uncertainties on the data markers are statistical, while the grey band shows the total statistical and systematic uncertainty.

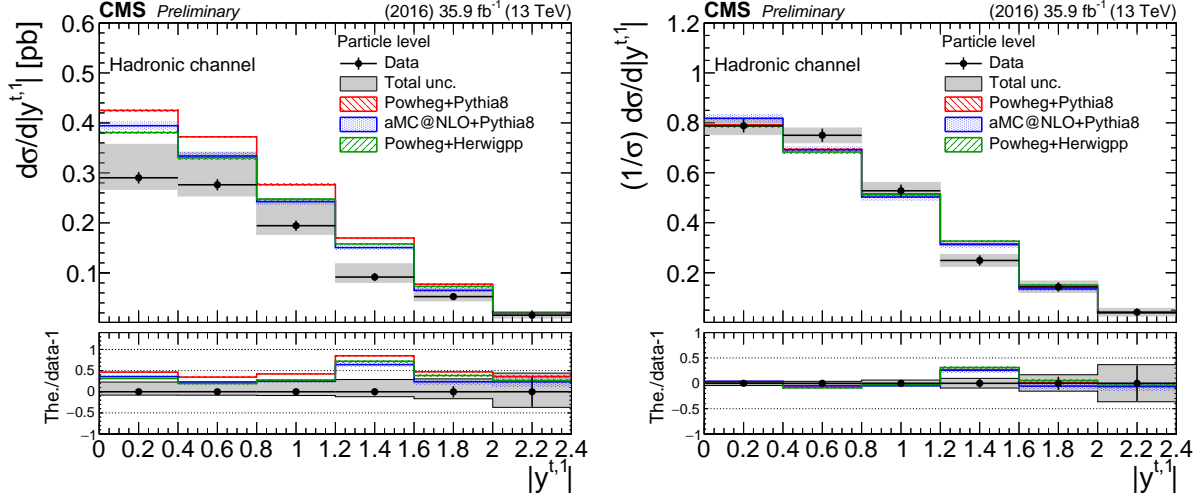


Figure 16: Differential cross section unfolded to the particle level, absolute (left) and normalized (right), as a function of the leading top quark  $|y|$  in the hadronic channel. The bottom panel shows the ratio (theory – data)/data. The uncertainties on the data markers are statistical, while the grey band shows the total statistical and systematic uncertainty.

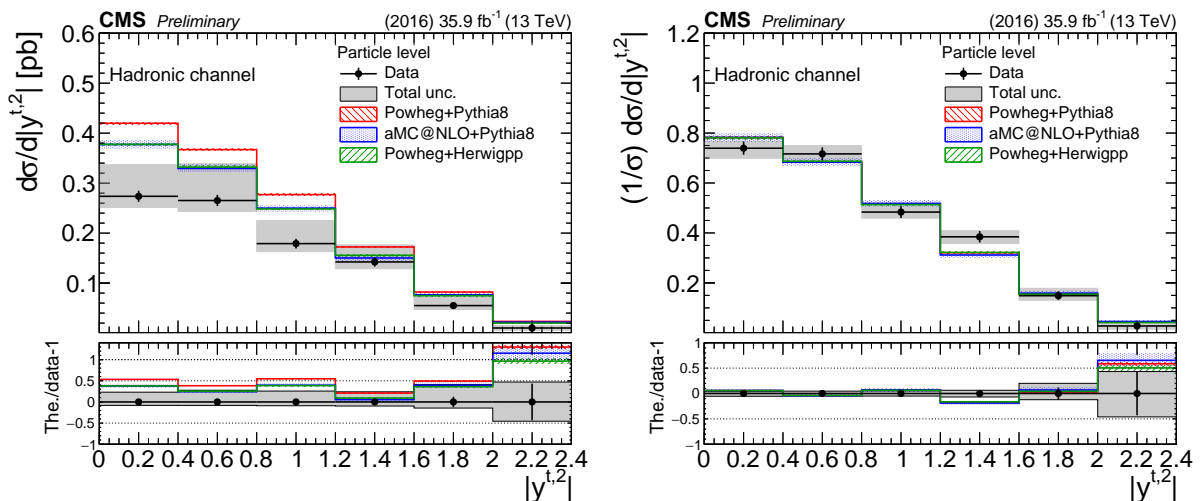


Figure 17: Differential cross section unfolded to the particle level, absolute (left) and normalized (right), as a function of the second top quark  $|y|$  in the hadronic channel. The bottom panel shows the ratio (theory – data)/data. The uncertainties on the data markers are statistical, while the grey band shows the total statistical and systematic uncertainty.

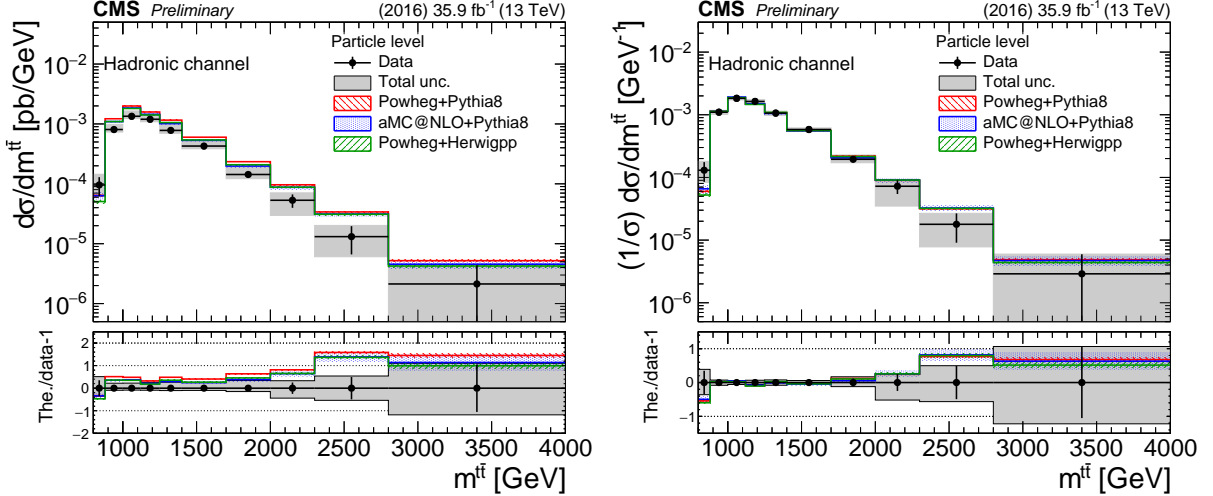


Figure 18: Differential cross section unfolded to the particle level, absolute (left) and normalized (right), as a function of  $m_{t\bar{t}}$  in the hadronic channel. The bottom panel shows the ratio (theory – data)/data. The uncertainties on the data markers are statistical, while the grey band shows the total statistical and systematic uncertainty.

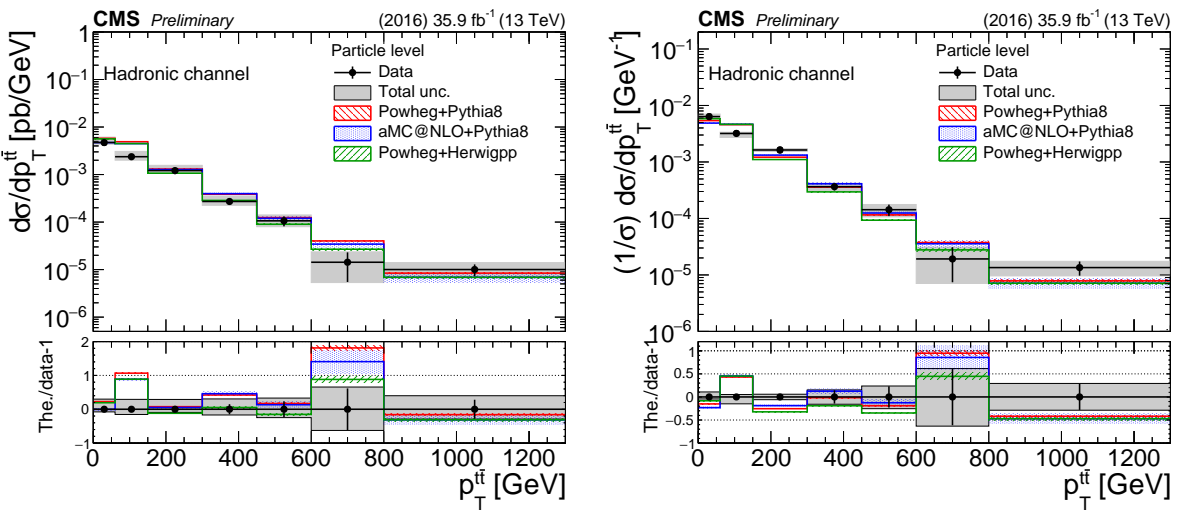


Figure 19: Differential cross section unfolded to the particle level, absolute (left) and normalized (right), as a function of  $p_T^{t\bar{t}}$  in the hadronic channel. The bottom panel shows the ratio (theory – data)/data. The uncertainties on the data markers are statistical, while the grey band shows the total statistical and systematic uncertainty.

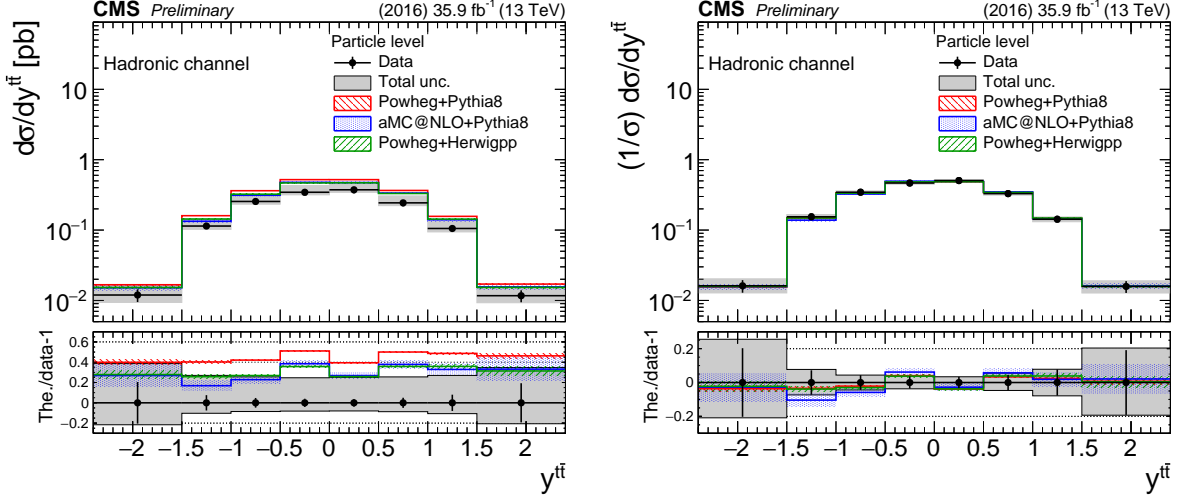


Figure 20: Differential cross section unfolded to the particle level, absolute (left) and normalized (right), as a function of  $y^{t\bar{t}}$  in the hadronic channel. The bottom panel shows the ratio (theory – data)/data. The uncertainties on the data markers are statistical, while the grey band shows the total statistical and systematic uncertainty.

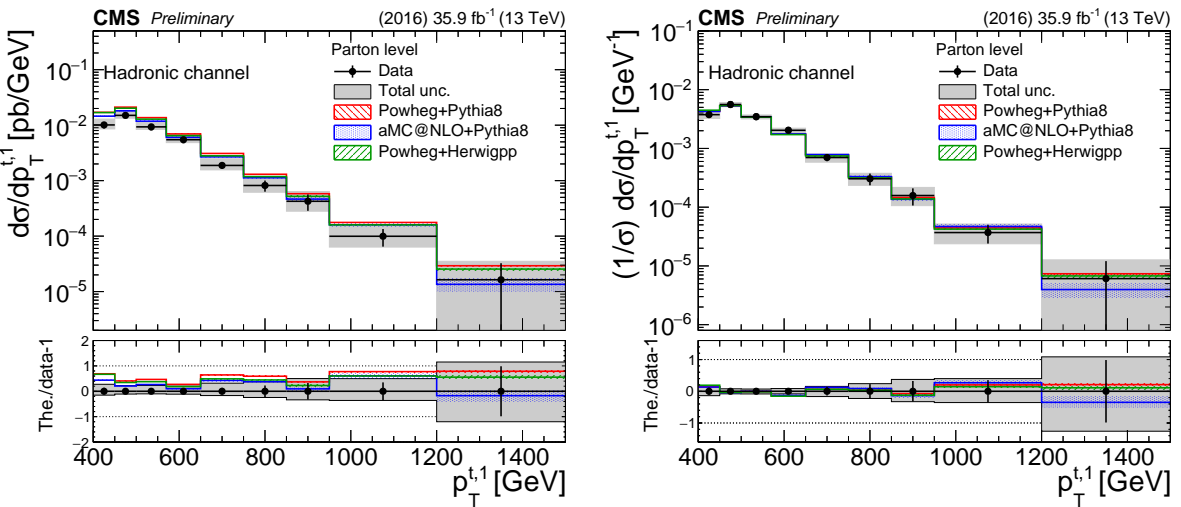


Figure 21: Differential cross section unfolded to the parton level, absolute (left) and normalized (right), as a function of the leading top quark  $p_T$  in the hadronic channel. The bottom panel shows the ratio (theory – data)/data. The uncertainties on the data markers are statistical, while the grey band shows the total statistical and systematic uncertainty.

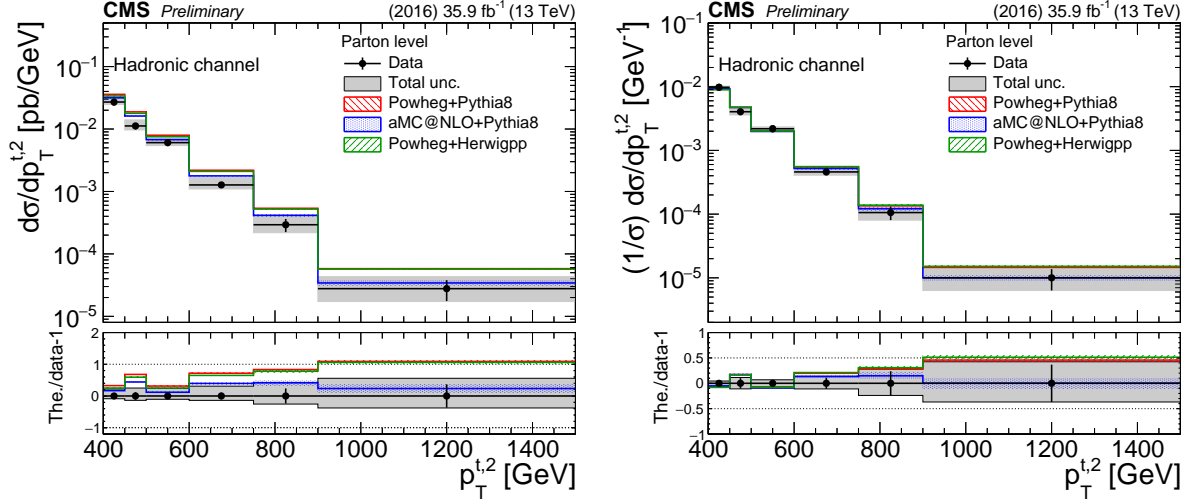


Figure 22: Differential cross section unfolded to the parton level, absolute (left) and normalized (right), as a function of the second top quark  $p_T$  in the hadronic channel. The bottom panel shows the ratio (theory – data)/data. The uncertainties on the data markers are statistical, while the grey band shows the total statistical and systematic uncertainty.

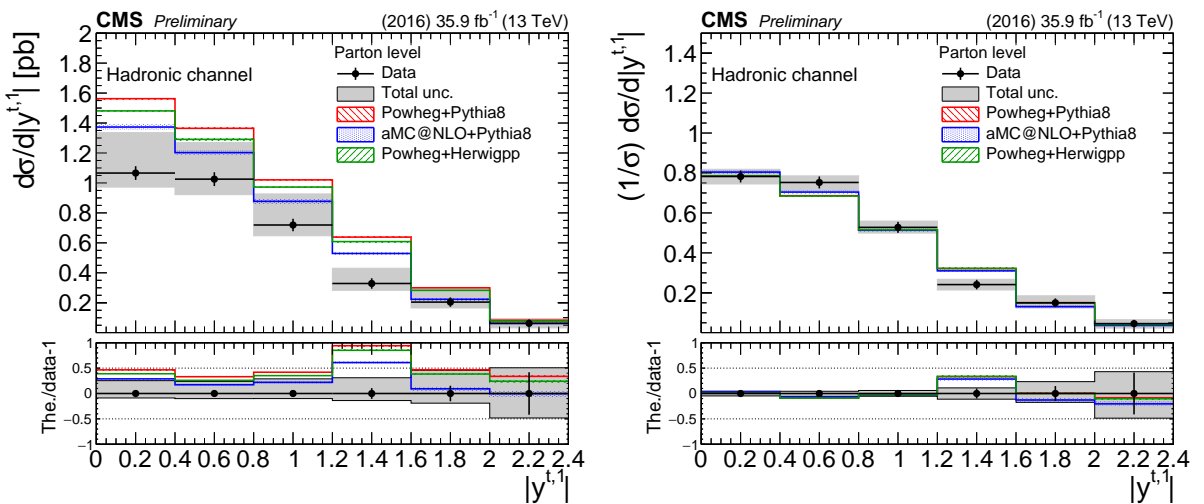


Figure 23: Differential cross section unfolded to the parton level, absolute (left) and normalized (right), as a function of the leading top  $|y|$  in the hadronic channel. The bottom panel shows the ratio (theory – data)/data. The uncertainties on the data markers are statistical, while the grey band shows the total statistical and systematic uncertainty.

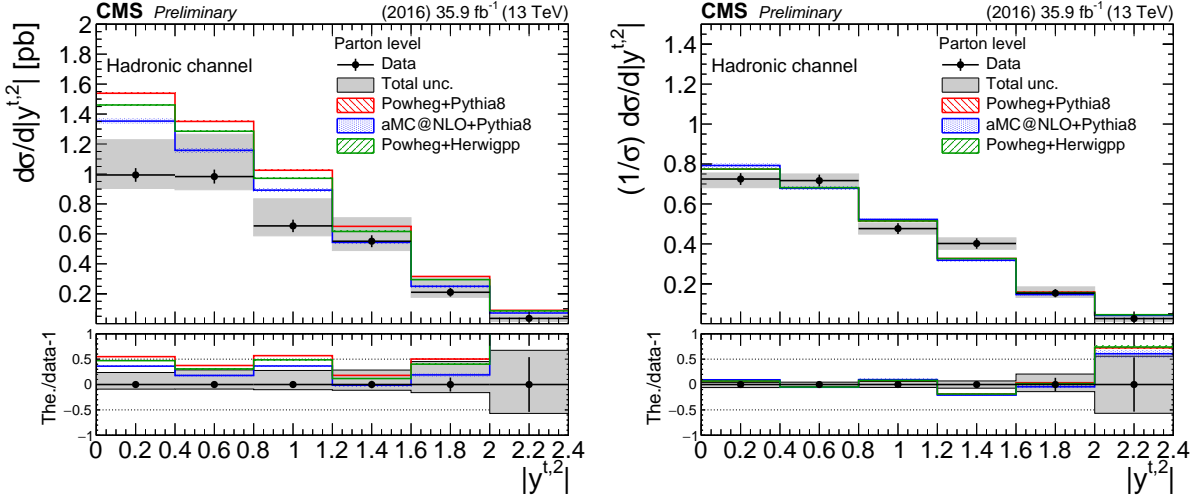


Figure 24: Differential cross section unfolded to the parton level, absolute (left) and normalized (right), as a function of the second top quark  $|y|$  in the hadronic channel. The bottom panel shows the ratio (theory – data)/data. The uncertainties on the data markers are statistical, while the grey band shows the total statistical and systematic uncertainty.

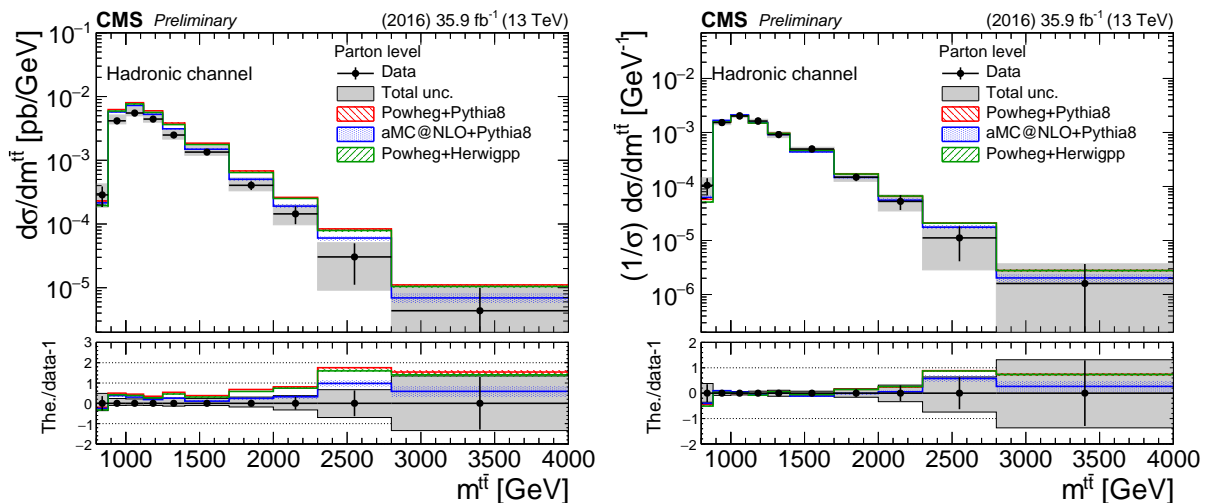


Figure 25: Differential cross section unfolded to the parton level, absolute (left) and normalized (right), as a function of  $m_{t\bar{t}}$  in the hadronic channel. The bottom panel shows the ratio (theory – data)/data. The uncertainties on the data markers are statistical, while the grey band shows the total statistical and systematic uncertainty.

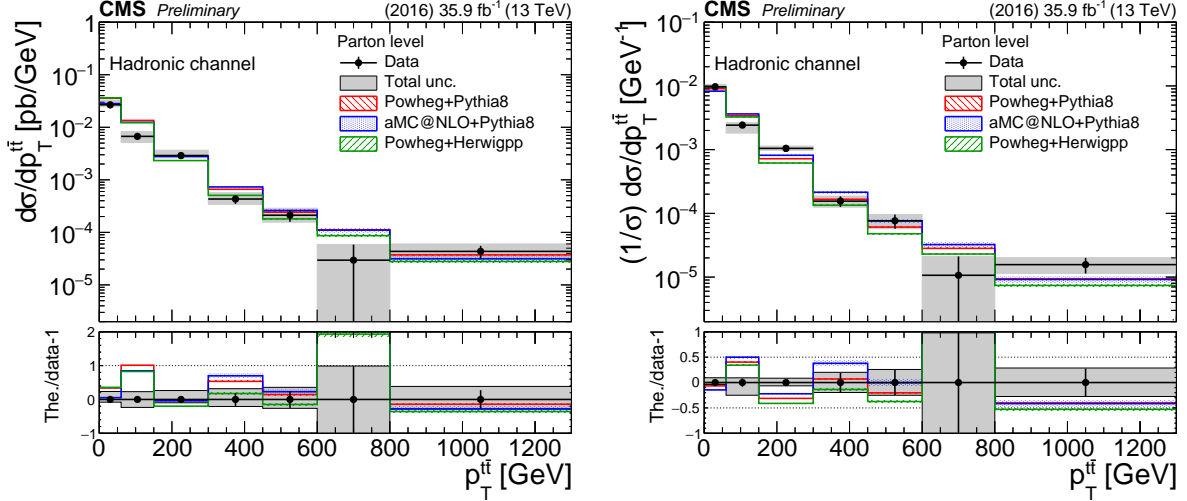


Figure 26: Differential cross section unfolded to the parton level, absolute (left) and normalized (right), as a function of  $p_T^{t\bar{t}}$  in the hadronic channel. The bottom panel shows the ratio (theory – data)/data. The uncertainties on the data markers are statistical, while the grey band shows the total statistical and systematic uncertainty.

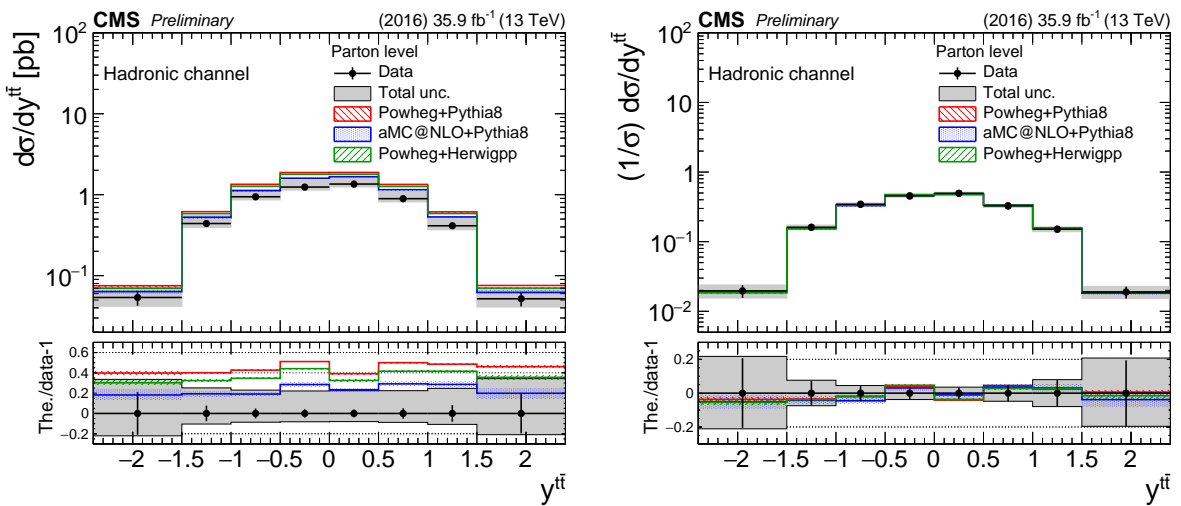


Figure 27: Differential cross section unfolded to the parton level, absolute (left) and normalized (right), as a function of  $y^{t\bar{t}}$  in the hadronic channel. The bottom panel shows the ratio (theory – data)/data. The uncertainties on the data markers are statistical, while the grey band shows the total statistical and systematic uncertainty.

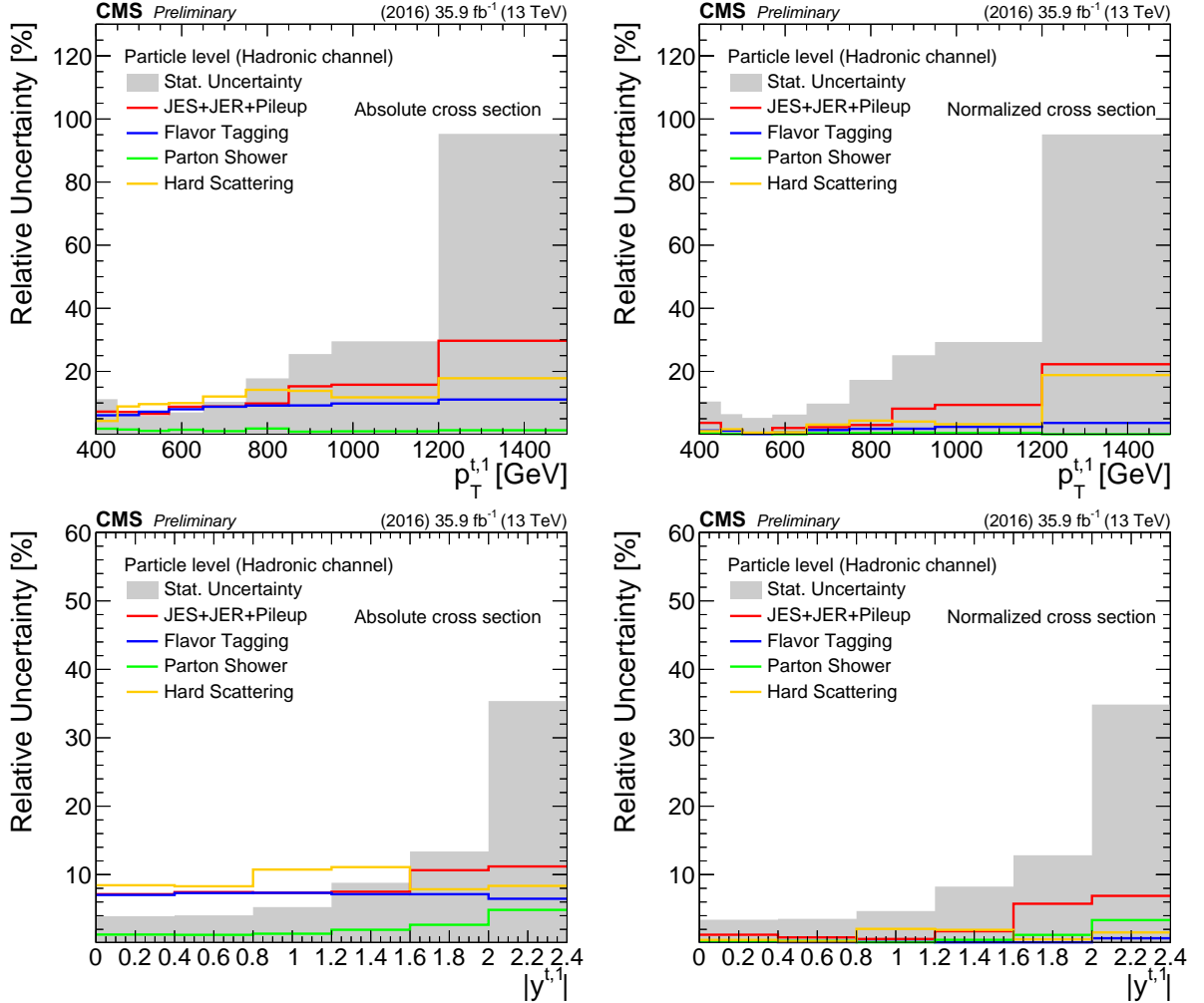


Figure 28: Decomposition of uncertainties in the absolute (left) and normalized (right) measurements at the particle level as a function of the leading top quark  $p_T$  (top) and  $|y|$  (bottom) in the hadronic channel. The grey band shows the statistical uncertainty, while the solid lines show the systematic uncertainties grouped in four categories: a) uncertainty due to pileup and the jet energy scale and resolution of the large- $R$  jets, b) uncertainty due to flavor tagging of the subjets, c) uncertainty due to the modeling of the parton shower, and d) uncertainty due to the modeling of the hard scattering.

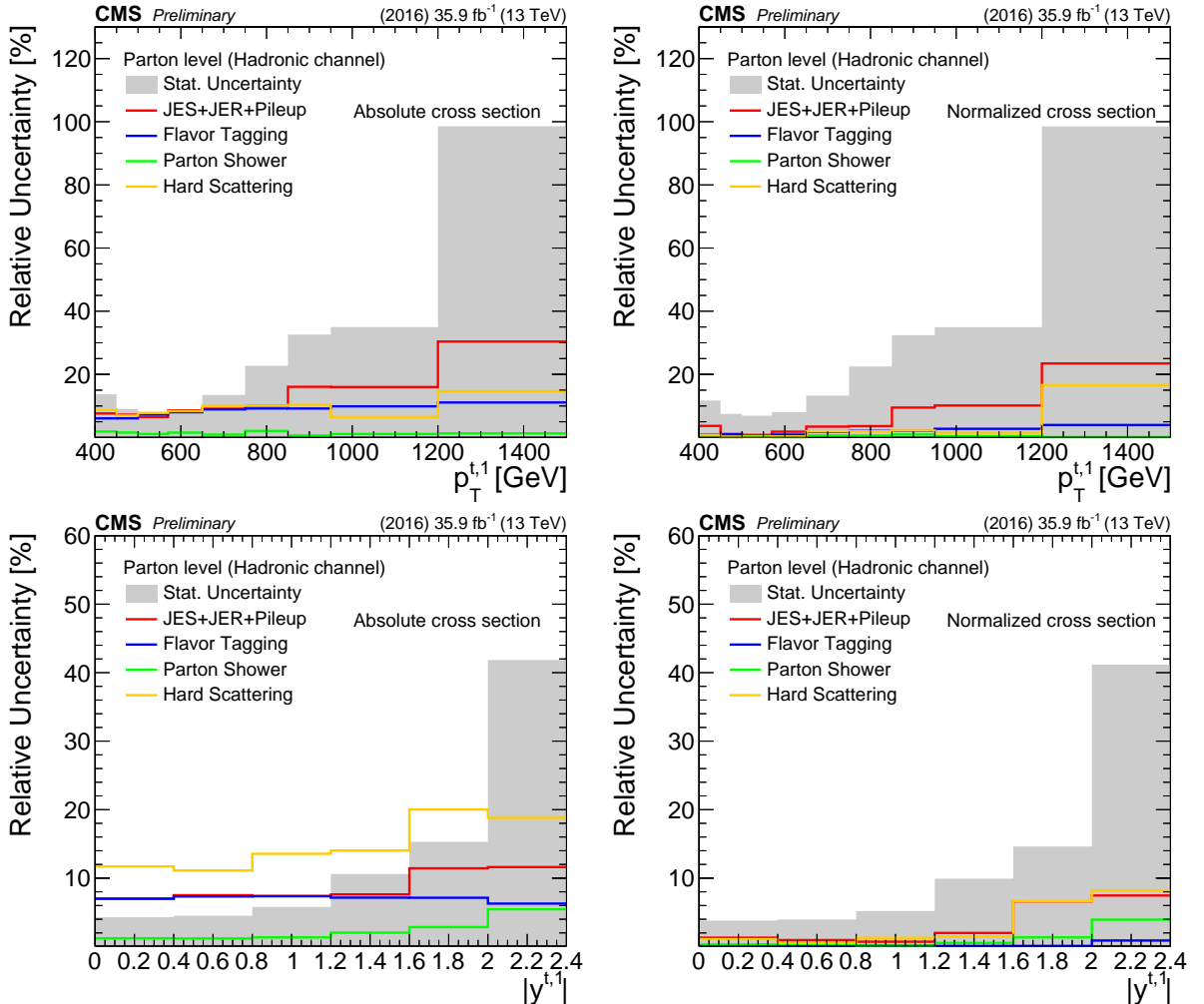


Figure 29: Decomposition of uncertainties in the absolute (left) and normalized (right) measurements at the parton level as a function of the leading top quark  $p_T$  (top) and  $|y|$  (bottom) in the hadronic channel. The grey band shows the statistical uncertainty, while the solid lines show the systematic uncertainties grouped in four categories: a) uncertainty due to pileup and the jet energy scale and resolution of the large- $R$  jets, b) uncertainty due to flavor tagging of the subjets, c) uncertainty due to the modeling of the parton shower, and d) uncertainty due to the modeling of the hard scattering.

#### 8.4 Lepton+jets channel

In the  $\ell$ +jets channel, the differential  $t\bar{t}$  cross section is measured as a function of the  $p_T$  and  $|y|$  of the hadronically decaying top quark. The measurement is performed at the particle level within a region of phase space mimicking the event selection criteria, as well as at the parton level within the full phase space. Semileptonic  $t\bar{t}$  events are selected at the parton level, and the properties of the hadronically decaying top quark are defined to represent the true top quark  $p_T$ .

The differential cross section is extracted from the signal-dominated 1t1b category. The measured signal distribution is determined by subtracting the estimated background contributions from the distribution in data, using the posterior normalizations from the fit given in Table 3. To account for signal reconstruction efficiencies and bin migrations, an unfolding procedure based on a least-squares minimization with Tikhonov regularization, as implemented in the TUNFOLD framework, is applied [56]. An unregularized unfolding was found to be optimal for the measurement. The unfolding relies on response matrices that map the  $p_T$  and  $|y|$  distributions for the  $t$ -tagged jet to corresponding properties for either the particle-level  $t$  jet candidate or the parton-level top quark.

The systematic uncertainty in the unfolded measurement receives contributions from experimental and theoretical sources, discussed in Section 7. The posterior values from the likelihood fit are used for the  $t$  tagging efficiency, background normalizations, and lepton efficiencies, while the *a priori* values are used for the remaining uncertainties. For each systematic variation that affects the shape of the  $p_T$  or  $|y|$  distribution, a separate response matrix is created that is used to unfold the data. The resulting uncertainties are added in quadrature to obtain the total uncertainty for the unfolded distribution.

The electron and muon channels are combined before the unfolding by merging the measured distributions as well as the response matrices for the two channels. The background contributions are also merged before subtracting these from the measured distributions, with the exception of the electron and muon QCD multijet backgrounds that are treated as separate sources.

The unfolded cross section results are shown in Figs. 30–33 as a function of  $p_T$  and  $|y|$  for the particle and parton level, respectively. The measurements are compared to the prediction from POWHEG+PYTHIA 8. The breakdown of the sources of systematic uncertainty are shown in Figs. 34 and 35. The unfolded cross section as a function of the  $p_T$  of the hadronically decaying top quark at the parton level that is presented in this note can additionally be compared to the corresponding measurement from the CMS Collaboration in the resolved final state [16]. The two measurements are observed to be in agreement in the region of phase space where they overlap.

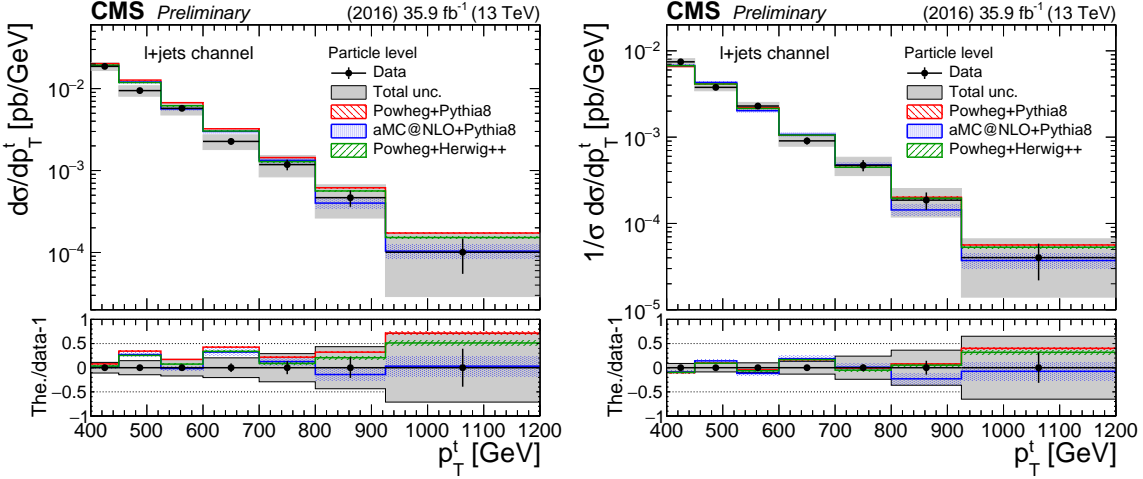


Figure 30: Differential cross section measurements at the particle level as a function of the particle-level  $t$  jet  $p_T$  for the  $\ell + \text{jets}$  channel. Both absolute (left) and normalized (right) cross sections are shown. The uncertainties on the data markers are statistical, while the grey band shows the total statistical and systematic uncertainty.

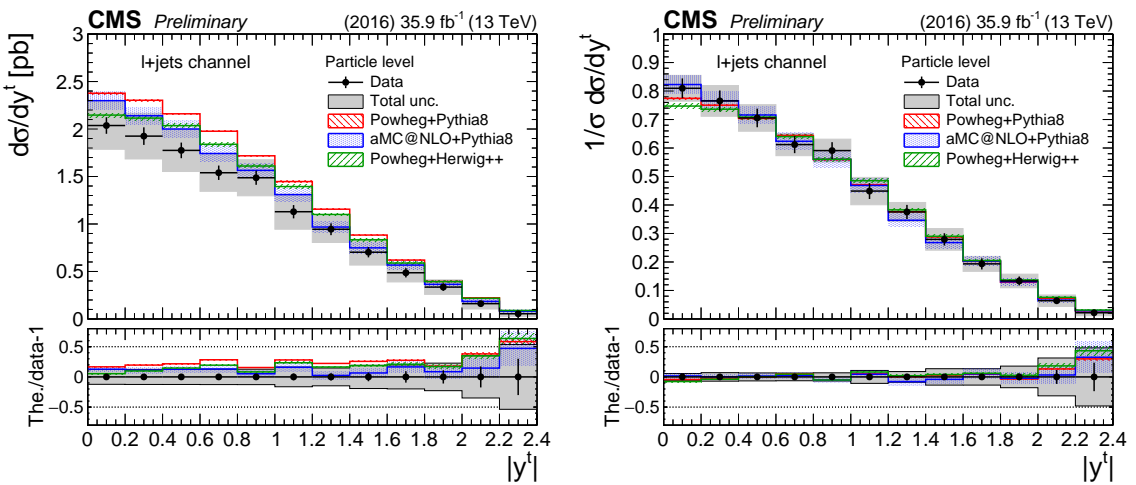


Figure 31: Differential cross section measurements at the particle level as a function of the particle-level  $t$  jet  $|y|$  for the  $\ell + \text{jets}$  channel. Both absolute (left) and normalized (right) cross sections are shown. The uncertainties on the data markers are statistical, while the grey band shows the total statistical and systematic uncertainty.

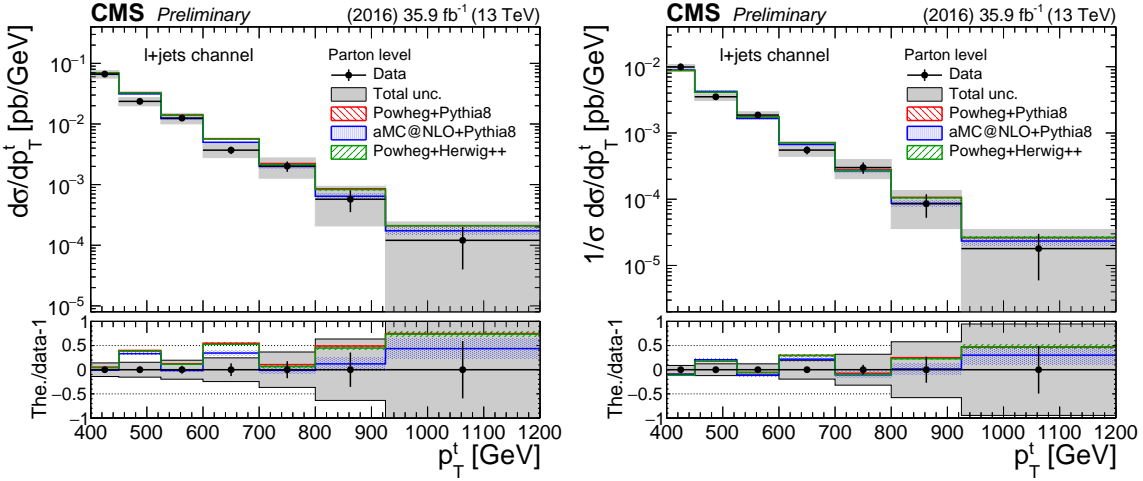


Figure 32: Differential cross section measurements at the parton level as a function of the parton-level top quark  $p_T$  for the  $\ell$ +jets channel. Both absolute (left) and normalized (right) cross sections are shown. The uncertainties on the data markers are statistical, while the grey band shows the total statistical and systematic uncertainty.

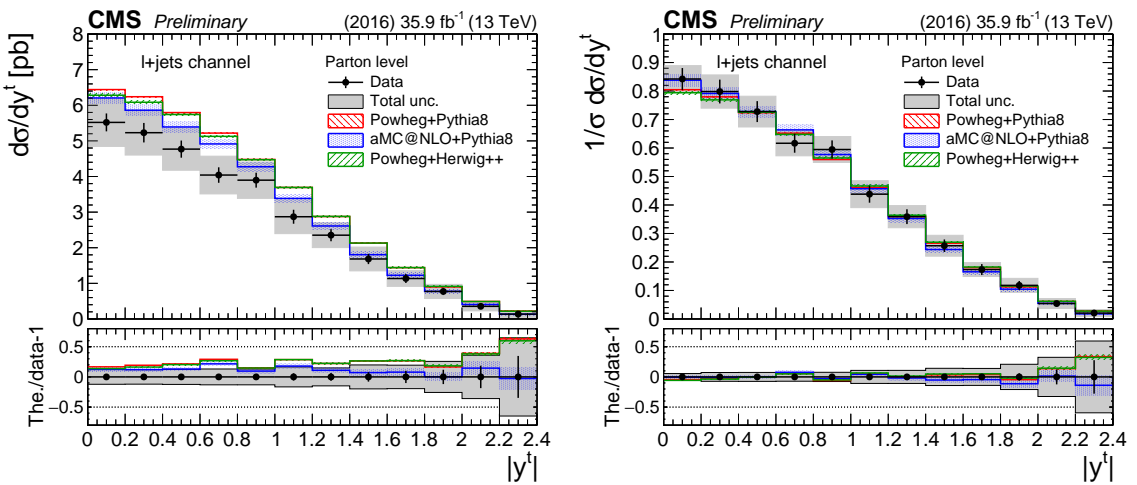


Figure 33: Differential cross section measurements at the parton level as a function of the parton-level top quark  $|y|$  for the  $\ell$ +jets channel. Both absolute (left) and normalized (right) cross sections are shown. The uncertainties on the data markers are statistical, while the grey band shows the total statistical and systematic uncertainty.

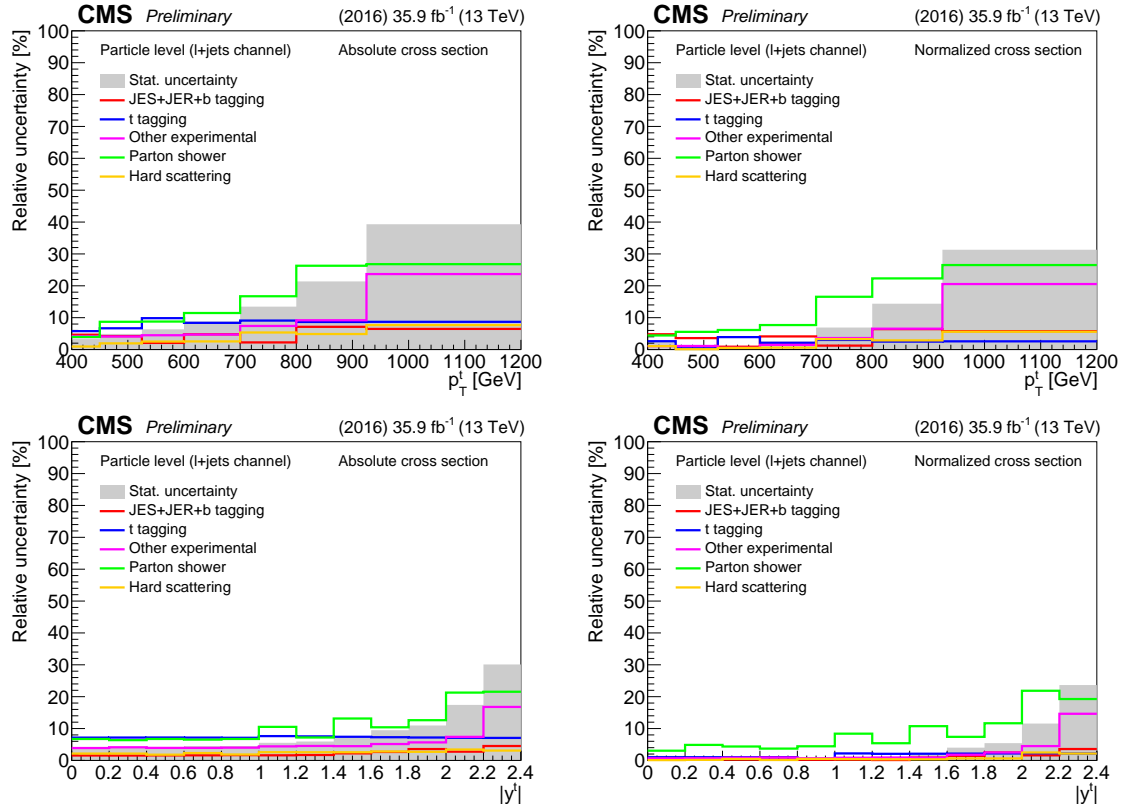


Figure 34: Breakdown of the sources of systematic uncertainty affecting the differential cross section measurements in the  $\ell$ +jets channel at the particle level as a function of the particle-level  $t$  jet  $p_T$  (top row) or  $|y|$  (bottom row). Both the systematic uncertainties in the absolute (left column) and the normalized (right column) cross sections are shown. "JES+JER+b tagging" includes uncertainties due to the jet energy scale, jet energy resolution, and small- $R$  jet  $b$  tagging efficiency; " $t$  tagging" is the uncertainty associated with the large- $R$  jet  $t$  tagging efficiency; "Other experimental" includes the uncertainties originating from the background estimate, pileup modeling, lepton identification and trigger efficiency, and measurement of the integrated luminosity; "Parton shower" includes contributions from initial- and final-state radiation, underlying event tune, ME-PS matching, and color reconnection; "Hard scattering" includes the uncertainty due to PDFs as well as renormalization and factorization scales.

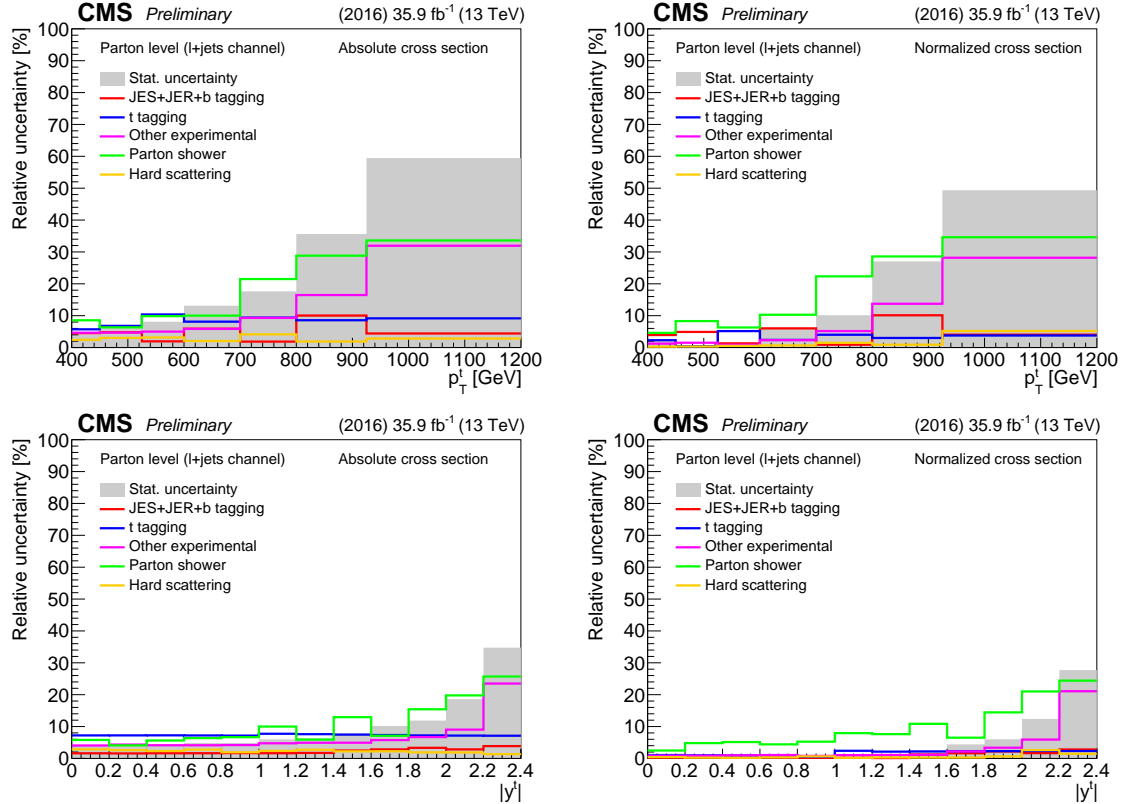


Figure 35: Breakdown of the sources of systematic uncertainty affecting the differential cross section measurements in the  $\ell+jets$  channel at the parton level as a function of the top quark  $p_T$  (top row) or  $|y|$  (bottom row). Both the systematic uncertainties in the absolute (left column) and the normalized (right column) cross sections are shown. "JES+JER+b tagging" includes uncertainties due to the jet energy scale, jet energy resolution, and small- $R$  jet b tagging efficiency; "t tagging" is the uncertainty associated with the large- $R$  jet t tagging efficiency; "Other experimental" includes the uncertainties originating from the background estimate, pileup modeling, lepton identification and trigger efficiency, and measurement of the integrated luminosity; "Parton shower" includes contributions from initial- and final-state radiation, underlying event tune, ME-PS matching, and color reconnection; "Hard scattering" includes the uncertainty due to PDFs as well as renormalization and factorization scales.

## 8.5 Discussion

The unfolded cross sections at the particle and parton level presented in Section 8 reveal some interesting features. First, there is a significant overestimate of the integrated cross section by about 35 (25)% in the hadronic ( $\ell$ +jets) channel, which is also in agreement with previous results [17]. In terms of the normalized differential cross section distributions, there is good agreement between the data and theory predictions for the leading top quark (hadronic channel) and the hadronically decaying top quark ( $\ell$ +jets channel)  $p_T$ , while the cross section as a function of the second top  $p_T$  (hadronic channel) appears to be softer in data for the POWHEG predictions with MC@NLO providing the best description. The  $y$  distributions are described well by the theory predictions in both channels. Finally, the measured  $t\bar{t}$  system kinematic distributions are in agreement with the theory prediction, with a possible deviation in the  $m_{t\bar{t}}$  variable, where POWHEG tends to produce a harder spectrum while MC@NLO is fully consistent with the data. Regarding the systematic uncertainties, it should be noted that they are in general larger for the hadronic channel because the two leading experimental sources, due to the jet energy scale and the b tagging, enter twice (two large- $R$  jets). In contrast, the parton-shower uncertainty is smaller for the hadronic channel because its main contribution (FSR) is constrained through a dedicated analysis, as explained in Section 7.

## 9 Summary

A measurement of the  $t\bar{t}$  production cross section for high- $p_T$  top quarks in proton-proton collisions at 13 TeV has been presented. The measurement uses events where either one or both top quarks decay hadronically, and where the hadronic decay products cannot be resolved but are instead clustered in a single large- $R$  jet with  $p_T > 400$  GeV. The hadronic final state contains two such large- $R$  jets, while the  $\ell$ +jets final state is identified through the presence of an electron/muon, a b-tagged jet from the leptonically decaying top quark, missing transverse momentum from the escaping neutrino, and a single t-tagged large- $R$  jet. The measurement utilizes a larger data set compared to previous results in order to explore a wider phase space of the  $t\bar{t}$  production and elucidate the discrepancies with the theory predictions that have been reported in earlier publications. For the hadronic channel, absolute and normalized differential cross sections are presented as a function of the leading and subleading top quark  $p_T$  and  $|y|$ , and as a function of the invariant mass,  $p_T$ , and  $y$  of the  $t\bar{t}$  system, unfolded to the particle and parton level. For the  $\ell$ +jets channel, the differential cross section is measured as a function of the  $p_T$  and  $|y|$  of the hadronically decaying top quark, at the particle level within a fiducial phase space and at the parton level. The results are compared to theoretical predictions from the POWHEG matrix-element generator, interfaced with PYTHIA8 or HERWIG++ for the underlying event and parton shower, and from the MC@NLO matrix-element generator, interfaced with PYTHIA8. All the models overpredict significantly the absolute cross section in the phase space of the measurement (by up to 35%), while they describe consistently the differential distribution of most variables. The most notable discrepancy is observed for the hadronic channel in the invariant mass of the  $t\bar{t}$  system and the  $p_T$  of the subleading t jet, where the theoretical models predict a higher cross section at high mass and  $p_T$  values, respectively. To further investigate the severity of this discrepancy, more data is needed to enhance the statistical significance of the measurement in this region of phase space.

## References

- [1] ATLAS Collaboration, "Measurements of top-quark pair differential cross-sections in the

- lepton+jets channel in  $pp$  collisions at  $\sqrt{s} = 13$  TeV using the ATLAS detector”, *JHEP* **11** (2017) 191, doi:[10.1007/JHEP11\(2017\)191](https://doi.org/10.1007/JHEP11(2017)191), arXiv:[1708.00727](https://arxiv.org/abs/1708.00727).
- [2] ATLAS Collaboration, “Measurements of top-quark pair differential cross-sections in the  $e\mu$  channel in  $pp$  collisions at  $\sqrt{s} = 13$  TeV using the ATLAS detector”, *Eur. Phys. J. C* **77** (2017) 292, doi:[10.1140/epjc/s10052-017-4821-x](https://doi.org/10.1140/epjc/s10052-017-4821-x), arXiv:[1612.05220](https://arxiv.org/abs/1612.05220).
- [3] ATLAS Collaboration, “Measurement of lepton differential distributions and the top quark mass in  $t\bar{t}$  production in  $pp$  collisions at  $\sqrt{s} = 8$  TeV with the ATLAS detector”, *Eur. Phys. J. C* **77** (2017) 804, doi:[10.1140/epjc/s10052-017-5349-9](https://doi.org/10.1140/epjc/s10052-017-5349-9), arXiv:[1709.09407](https://arxiv.org/abs/1709.09407).
- [4] ATLAS Collaboration, “Measurement of top quark pair differential cross-sections in the dilepton channel in  $pp$  collisions at  $\sqrt{s} = 7$  and 8 TeV with ATLAS”, *Phys. Rev. D* **94** (2016) 092003, doi:[10.1103/PhysRevD.94.092003](https://doi.org/10.1103/PhysRevD.94.092003), arXiv:[1607.07281](https://arxiv.org/abs/1607.07281).
- [5] ATLAS Collaboration, “Differential top-antitop cross-section measurements as a function of observables constructed from final-state particles using  $pp$  collisions at  $\sqrt{s} = 7$  TeV in the ATLAS detector”, *JHEP* **06** (2015) 100, doi:[10.1007/JHEP06\(2015\)100](https://doi.org/10.1007/JHEP06(2015)100), arXiv:[1502.05923](https://arxiv.org/abs/1502.05923).
- [6] ATLAS Collaboration, “Measurements of top quark pair relative differential cross-sections with ATLAS in  $pp$  collisions at  $\sqrt{s} = 7$  TeV”, *Eur. Phys. J. C* **73** (2013) 2261, doi:[10.1140/epjc/s10052-012-2261-1](https://doi.org/10.1140/epjc/s10052-012-2261-1), arXiv:[1207.5644](https://arxiv.org/abs/1207.5644).
- [7] CMS Collaboration, “Measurement of normalized differential  $t\bar{t}$  cross sections in the dilepton channel from  $pp$  collisions at  $\sqrt{s} = 13$  TeV”, *JHEP* **04** (2018) 060, doi:[10.1007/JHEP04\(2018\)060](https://doi.org/10.1007/JHEP04(2018)060), arXiv:[1708.07638](https://arxiv.org/abs/1708.07638).
- [8] CMS Collaboration, “Measurements of normalised multi-differential cross sections for top quark pair production in  $pp$  collisions at  $\sqrt{s} = 13$  TeV and simultaneous determination of the strong coupling strength, top quark pole mass and parton distribution functions”, (2019). arXiv:[1904.05237](https://arxiv.org/abs/1904.05237). Submitted to *Eur. Phys. J.*
- [9] CMS Collaboration, “Measurements of  $t\bar{t}$  differential cross sections in proton-proton collisions at  $\sqrt{s} = 13$  TeV using events containing two leptons”, *JHEP* **02** (2019) 149, doi:[10.1007/JHEP02\(2019\)149](https://doi.org/10.1007/JHEP02(2019)149), arXiv:[1811.06625](https://arxiv.org/abs/1811.06625).
- [10] CMS Collaboration, “Measurement of differential cross sections for top quark pair production using the lepton+jets final state in proton-proton collisions at 13 TeV”, *Phys. Rev. D* **95** (2017) 092001, doi:[10.1103/PhysRevD.95.092001](https://doi.org/10.1103/PhysRevD.95.092001), arXiv:[1610.04191](https://arxiv.org/abs/1610.04191).
- [11] CMS Collaboration, “Measurements of differential cross sections of top quark pair production as a function of kinematic event variables in proton-proton collisions at  $\sqrt{s} = 13$  TeV”, *JHEP* **06** (2018) 002, doi:[10.1007/JHEP06\(2018\)002](https://doi.org/10.1007/JHEP06(2018)002), arXiv:[1803.03991](https://arxiv.org/abs/1803.03991).
- [12] CMS Collaboration, “Measurement of double-differential cross sections for top quark pair production in  $pp$  collisions at  $\sqrt{s} = 8$  TeV and impact on parton distribution functions”, *Eur. Phys. J. C* **77** (2017) 459, doi:[10.1140/epjc/s10052-017-4984-5](https://doi.org/10.1140/epjc/s10052-017-4984-5), arXiv:[1703.01630](https://arxiv.org/abs/1703.01630).
- [13] CMS Collaboration, “Measurement of the differential cross section for top quark pair production in  $pp$  collisions at  $\sqrt{s} = 8$  TeV”, *Eur. Phys. J. C* **75** (2015) 542, doi:[10.1140/epjc/s10052-015-3709-x](https://doi.org/10.1140/epjc/s10052-015-3709-x), arXiv:[1505.04480](https://arxiv.org/abs/1505.04480).

- [14] CMS Collaboration, “Measurement of the differential cross sections for top quark pair production as a function of kinematic event variables in pp collisions at  $\sqrt{s} = 7$  and 8 TeV”, *Phys. Rev. D* **94** (2016) 052006, doi:10.1103/PhysRevD.94.052006, arXiv:1607.00837.
- [15] CMS Collaboration, “Measurement of differential top-quark pair production cross sections in pp collisions at  $\sqrt{s} = 7$  TeV”, *Eur. Phys. J. C* **73** (2013) 2339, doi:10.1140/epjc/s10052-013-2339-4, arXiv:1211.2220.
- [16] CMS Collaboration, “Measurement of differential cross sections for the production of top quark pairs and of additional jets in lepton+jets events from pp collisions at  $\sqrt{s} = 13$  TeV”, *Phys. Rev. D* **97** (2018) 112003, doi:10.1103/PhysRevD.97.112003, arXiv:1803.08856.
- [17] ATLAS Collaboration, “Measurements of  $t\bar{t}$  differential cross-sections of highly boosted top quarks decaying to all-hadronic final states in  $pp$  collisions at  $\sqrt{s} = 13$  TeV using the ATLAS detector”, *Phys. Rev. D* **98** (2018) 012003, doi:10.1103/PhysRevD.98.012003, arXiv:1801.02052.
- [18] ATLAS Collaboration, “Measurement of the differential cross-section of highly boosted top quarks as a function of their transverse momentum in  $\sqrt{s} = 8$  TeV proton-proton collisions using the ATLAS detector”, *Phys. Rev. D* **93** (2016) 032009, doi:10.1103/PhysRevD.93.032009, arXiv:1510.03818.
- [19] CMS Collaboration, “Measurement of the integrated and differential  $t\bar{t}$  production cross sections for high- $p_t$  top quarks in  $pp$  collisions at  $\sqrt{s} = 8$  TeV”, *Phys. Rev. D* **94** (2016) 072002, doi:10.1103/PhysRevD.94.072002, arXiv:1605.00116.
- [20] P. Nason, “A new method for combining NLO QCD with shower Monte Carlo algorithms”, *JHEP* **11** (2004) 040, doi:10.1088/1126-6708/2004/11/040, arXiv:hep-ph/0409146.
- [21] S. Frixione, P. Nason, and G. Ridolfi, “A Positive-weight next-to-leading-order Monte Carlo for heavy flavour hadroproduction”, *JHEP* **09** (2007) 126, doi:10.1088/1126-6708/2007/09/126, arXiv:0707.3088.
- [22] S. Frixione, P. Nason, and C. Oleari, “Matching NLO QCD computations with parton shower simulations: the POWHEG method”, *JHEP* **11** (2007) 070, doi:10.1088/1126-6708/2007/11/070, arXiv:0709.2092.
- [23] S. Alioli, P. Nason, C. Oleari, and E. Re, “A general framework for implementing NLO calculations in shower Monte Carlo programs: the POWHEG BOX”, *JHEP* **06** (2010) 043, doi:10.1007/JHEP06(2010)043, arXiv:1002.2581.
- [24] S. Alioli, S. O. Moch, and P. Uwer, “Hadronic top-quark pair-production with one jet and parton showering”, *JHEP* **01** (2012) 137, doi:10.1007/JHEP01(2012)137, arXiv:1110.5251.
- [25] S. Alioli, P. Nason, C. Oleari, and E. Re, “NLO single-top production matched with shower in POWHEG:  $s$ - and  $t$ -channel contributions”, *JHEP* **09** (2009) 111, doi:10.1088/1126-6708/2009/09/111, arXiv:0907.4076. [Erratum: doi:10.1007/JHEP02(2010)011].

- [26] J. Alwall et al., “The automated computation of tree-level and next-to-leading order differential cross sections, and their matching to parton shower simulations”, *JHEP* **07** (2014) 079, doi:10.1007/JHEP07(2014)079, arXiv:1405.0301.
- [27] J. Alwall et al., “Comparative study of various algorithms for the merging of parton showers and matrix elements in hadronic collisions”, *Eur. Phys. J. C* **53** (2008) 473, doi:10.1140/epjc/s10052-007-0490-5, arXiv:0706.2569.
- [28] T. Sjöstrand, S. Mrenna, and P. Z. Skands, “PYTHIA 6.4 physics and manual”, *JHEP* **05** (2006) 026, doi:10.1088/1126-6708/2006/05/026, arXiv:hep-ph/0603175.
- [29] T. Sjöstrand, S. Mrenna, and P. Z. Skands, “A brief introduction to PYTHIA 8.1”, *Comput. Phys. Commun.* **178** (2008) 852, doi:10.1016/j.cpc.2008.01.036, arXiv:0710.3820.
- [30] NNPDF Collaboration, “Parton distributions for the LHC Run II”, *JHEP* **04** (2015) 040, doi:10.1007/JHEP04(2015)040, arXiv:1410.8849.
- [31] CMS Collaboration, “Event generator tunes obtained from underlying event and multiparton scattering measurements”, *Eur. Phys. J. C* **76** (2015) 155, doi:10.1140/epjc/s10052-016-3988-x, arXiv:1512.00815.
- [32] CMS Collaboration, “Investigations of the impact of the parton shower tuning in Pythia 8 in the modelling of  $t\bar{t}$  at  $\sqrt{s} = 8$  and 13 TeV”, CMS Physics Analysis Summary CMS-PAS-TOP-16-021, 2016.
- [33] GEANT4 Collaboration, “GEANT4—a simulation toolkit”, *Nucl. Instrum. Meth. A* **506** (2003) 250, doi:10.1016/S0168-9002(03)01368-8.
- [34] M. Czakon and A. Mitov, “Top++: A program for the calculation of the top-pair cross-section at hadron colliders”, *Comput. Phys. Commun.* **185** (2014) 2930, doi:10.1016/j.cpc.2014.06.021, arXiv:1112.5675.
- [35] Y. Li and F. Petriello, “Combining QCD and electroweak corrections to dilepton production in the framework of the FEWZ simulation code”, *Phys. Rev. D* **86** (2012) 094034, doi:10.1103/PhysRevD.86.094034, arXiv:1208.5967.
- [36] N. Kidonakis, “Top Quark Production”, (2014). arXiv:1311.0283.
- [37] M. Bahr et al., “Herwig++ Physics and Manual”, *Eur. Phys. J. C* **58** (2008) 639, doi:10.1140/epjc/s10052-008-0798-9, arXiv:0803.0883.
- [38] S. Gieseke, C. Rohr, and A. Siodmok, “Colour reconnections in Herwig++”, *Eur. Phys. J. C* **72** (2012) 2225, doi:10.1140/epjc/s10052-012-2225-5, arXiv:1206.0041.
- [39] CMS Collaboration, “Particle-flow reconstruction and global event description with the cms detector”, *JINST* **12** (2017) P10003, doi:10.1088/1748-0221/12/10/P10003, arXiv:1706.04965.
- [40] M. Cacciari, G. P. Salam, and G. Soyez, “The anti- $k_t$  jet clustering algorithm”, *JHEP* **04** (2008) 063, doi:10.1088/1126-6708/2008/04/063, arXiv:0802.1189.
- [41] M. Cacciari, G. P. Salam, and G. Soyez, “FastJet user manual”, *Eur. Phys. J. C* **72** (2012) 1896, doi:10.1140/epjc/s10052-012-1896-2, arXiv:1111.6097.

- [42] CMS Collaboration, “Jet energy scale and resolution in the CMS experiment in pp collisions at 8 TeV”, *JINST* **12** (2017) P02014, doi:10.1088/1748-0221/12/02/P02014, arXiv:1607.03663.
- [43] J. Thaler and K. Van Tilburg, “Identifying boosted objects with  $N$ -subjettiness”, *JHEP* **03** (2011) 015, doi:10.1007/JHEP03(2011)015, arXiv:1011.2268.
- [44] S. Catani, Y. L. Dokshitzer, M. H. Seymour, and B. R. Webber, “Longitudinally invariant  $K_t$  clustering algorithms for hadron-hadron collisions”, *Nucl. Phys. B* **406** (1993) 187, doi:10.1016/0550-3213(93)90166-M.
- [45] J. Thaler and K. Van Tilburg, “Maximizing Boosted Top Identification by Minimizing  $N$ -subjettiness”, *JHEP* **02** (2012) 093, doi:10.1007/JHEP02(2012)093, arXiv:1108.2701.
- [46] M. Dasgupta, A. Fregoso, S. Marzani, and G. P. Salam, “Towards an understanding of jet substructure”, *JHEP* **09** (2013) 029, doi:10.1007/JHEP09(2013)029, arXiv:1307.0007.
- [47] J. M. Butterworth, A. R. Davison, M. Rubin, and G. P. Salam, “Jet substructure as a new Higgs search channel at the LHC”, *Phys. Rev. Lett.* **100** (2008) 242001, doi:10.1103/PhysRevLett.100.242001, arXiv:0802.2470.
- [48] A. J. Larkoski, S. Marzani, G. Soyez, and J. Thaler, “Soft drop”, *JHEP* **05** (2014) 146, doi:10.1007/JHEP05(2014)146, arXiv:1402.2657.
- [49] Y. L. Dokshitzer, G. D. Leder, S. Moretti, and B. R. Webber, “Better jet clustering algorithms”, *JHEP* **08** (1997) 001, doi:10.1088/1126-6708/1997/08/001, arXiv:hep-ph/9707323.
- [50] M. Wobisch and T. Wengler, “Hadronization corrections to jet cross-sections in deep inelastic scattering”, in *Proceedings of the Workshop on Monte Carlo Generators for HERA Physics, Hamburg, Germany*, p. 270. 1998. arXiv:hep-ph/9907280.
- [51] CMS Collaboration, “Identification of heavy-flavour jets with the CMS detector in pp collisions at 13 TeV”, *JINST* **13** (2018) P05011, doi:10.1088/1748-0221/13/05/P05011, arXiv:1712.07158.
- [52] W. Verkerke and D. P. Kirkby, “The RooFit toolkit for data modeling”, *eConf* **C0303241** (2003) MOLT007, arXiv:physics/0306116.
- [53] ATLAS Collaboration, “Measurement of the Inelastic Proton-Proton Cross Section at  $\sqrt{s} = 13$  TeV with the ATLAS Detector at the LHC”, *Phys. Rev. Lett.* **117** (2016) 182002, doi:10.1103/PhysRevLett.117.182002, arXiv:1606.02625.
- [54] CMS Collaboration, “CMS Luminosity Measurements for the 2016 Data Taking Period”, CMS Physics Analysis Summary CMS-PAS-LUM-17-001, 2017.
- [55] P. Skands, S. Carrazza, and J. Rojo, “Tuning PYTHIA 8.1: the Monash 2013 tune”, *Eur. Phys. J. C* **74** (2014) 3024, doi:10.1140/epjc/s10052-014-3024-y, arXiv:1404.5630.
- [56] S. Schmitt, “TUnfold: an algorithm for correcting migration effects in high energy physics”, *JINST* **7** (2012) T10003, doi:10.1088/1748-0221/7/10/T10003, arXiv:1205.6201.